Computers and Geotechnics 202 (2027) 108619

Contents lists available at ScienceDirect

Computers and Geotechnics

journal homepage: www.elsevier.com/locate/compgeo

Research paper

Multi-scale modeling of wheel–terrain interactions for planetary rovers

Hao Chen [a], Shiwei Zhao [b],*, Jidong Zhao [a],*

[a] Department of Civil and Environmental Engineering, The Hong Kong University of Science and Technology, Hong Kong Special Administrative Region
[b] Institute of Water Engineering Sciences, Wuhan University, Wuhan, China

ARTICLE INFO

Keywords:
Granular materials
Wheel–terrain interaction
Multiscale modeling
Rover

ABSTRACT

Assessing the mobility and stability of off-road vehicles poses fundamental challenges, particularly in extraterrestrial environments. Current research relies primarily on experimental data and empirical models, while high-fidelity numerical simulations are hindered by the complexity of wheel–terrain interactions. These involve multiple length scales due to heterogeneous terrain materials such as sand, gravel, and rock. This paper presents a multiscale computational framework for wheel–terrain interaction that consistently captures coupled behavior across scales. Interactions involving wheel–rock, wheel–sand, and rock–sand are modeled using a nonlinear contact formulation that supports arbitrary geometries for both wheels and terrain constituents. The internal dynamics of the coupled system are resolved using the Discrete Element Method (DEM) and the Material Point Method (MPM), linked through a contact-coupling interface that enables accurate two-way transfer between discrete granular flow and large-deformation continuum response. A highly parallel computational strategy significantly improves scalability across DEM- or MPM-dominated contact regimes in high-resolution simulations. The framework is validated against analytical benchmarks, including head-on sphere collisions, wheel-drop tests, and rolling tests, to assess its quantitative predictive robustness. It is then applied to simulate two NASA Mars rover incidents: the permanent entrapment of *Spirit* and the excessive slip experienced by *Curiosity*. The framework demonstrates strong potential for realistic off-road applications, including mobility prediction, stability assessment, and post-incident analysis. In particular, for the *Spirit* case, material properties matched to observations are compiled to reproduce, as closely as possible, the normalized sinkage-slip trend and to compare it with published single-wheel measurements, thereby providing a partial quantitative analysis at field scale.

1. Introduction

Exploring other planets is driven by scientific, resource-related, and colonization goals (Green et al., 2021), with planetary rovers serving as the primary tool for investigation. Recent missions, such as NASA's *Perseverance* and CNSA's *Zhurong*, operate on unfamiliar terrain under significant communication delays, up to 40 min round-trip for Mars, which necessitates cautious driving and limits direct teleoperation. Autonomous navigation is thus critical for safer, faster, and longer traverses. While *Perseverance*'s enhanced autonomy allows for real-time route selection (Verma et al., 2023), it still requires operator input for hazard assessment, highlighting the need to overcome these limitations for full autonomy (Nesnas et al., 2021). Rovers face unique challenges beyond terrestrial driving, including radiation-hardened but low-performance processors (e.g., *Perseverance*'s 200 MHz PowerPC RAD750 (Farley et al., 2020)) and hazardous terrain. Abundant Martian sand has immobilized rovers such as *Opportunity*, *Spirit*, and *Curiosity* (Fig. 1(a–c)), while rugged terrain causes significant wheel damage (Fig. 1(d)), underscoring the need for improved vehicle resilience.

A deeper understanding of wheel–soil interaction is essential to enhance rover control, design, and longevity, necessitating a practical computational framework for modeling these interactions (Recuero et al., 2017). This framework must address three critical challenges. First, it must account for the discrete nature and complex, sharp particle morphology of planetary regolith, which differs markedly from weathered Earth soil and governs its mechanical properties (Kawamoto et al., 2018; J. Zhao et al., 2023). Second, it must capture the multi-scale nature of the interaction, from interparticle forces to the collective wheel response, a task complicated by irregular particle shapes. Third, it must manage the immense computational cost of such high-fidelity, multi-scale modeling. Existing studies often overlook these combined aspects, limiting model fidelity. A robust framework would form the basis for a high-fidelity rover simulator or digital twin, advancing the goal of fully autonomous planetary exploration (Tasora et al., 2015).

Advanced techniques such as machine learning have attracted increasing attention for their uses in route planning and auto-navigation (Daftry et al., 2022; Liu et al., 2023; Zhang et al., 2023). However,

* Corresponding authors.
E-mail addresses: swzhao@whu.edu.cn (S. Zhao), jzhao@ust.hk (J. Zhao).

https://doi.org/10.1016/j.compgeo.2026.108619
Received 13 July 2026; Received in revised form 24 August 2026; Accepted 31 August 2026

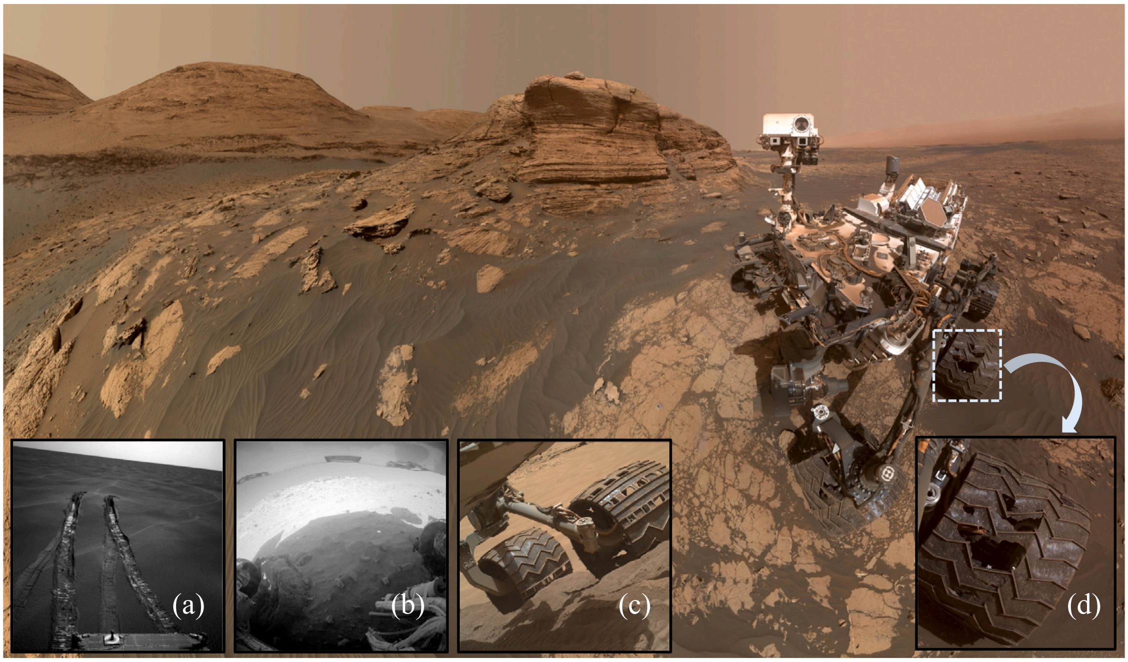

Fig. 1. Mars rovers: (a) The wheels of *Opportunity* dug more than 10 cm deep into the sandy material in 2005, (b) *Spirit* stuck in a sand pit in 2010, (c) *Curiosity* with its wheels deep in soft sand in 2014, and (d) The *Curiosity* rover at Mont Mercou with damaged wheels due to jagged rocks covered by sand in 2021. Image credit: NASA/JPL/MSSS.

without considering wheel–terrain interaction, the self-driving planetary rover must avoid extreme but often scientifically interesting terrain with sand traps, rocks, boulders and other hazardous obstacles (Farley et al., 2020; Li and Lewis, 2023; Wang et al., 2025). Incorporating knowledge of wheel–terrain interaction into self-driving can enable a rover to traverse extreme terrain safely. Specifically, with a wheel–terrain interaction model, it would be possible to estimate the in-situ geomechanical properties directly based on wheel tracks, as experimentally tried on CNSA's Mars rover *Zhurong* (Ding et al., 2022a). Wheel–terrain interaction also plays an important role in several other sectors, including wheel design and optimization, mobility control in an energy-efficient pace, rover simulation, and digital twin construction. Therefore, for viable, long-lived efficient self-driving planetary rovers, accurate understanding of wheel–terrain interaction is crucial. The numerical tool proposed here will be sufficiently general and robust enough to model wheel–terrain interaction with multi-scale considerations for engineering reference.

Pioneered by Bekker (1956) and Wong and Reece (1967), semi-empirical models of wheel–terrain interaction have been widely employed to study soil reactions in response to the wheel movement on earth (Mardani et al., 2020; Wang et al., 2020), and even for the estimation of in-situ geomechanical properties of Lunar or Martian soils (Ding et al., 2022a,b). Semi-empirical techniques can simplify any problem enough to make it easily solvable. In this case, however, those semi-empirical models introduce too many assumptions without considering the profile and dynamics of soil, the transient motion of the wheel (He et al., 2019; Peiret et al., 2021) or the reduced gravity (Niksirat et al., 2020). High-fidelity modeling of wheel–terrain interaction is challenged by the complicated collective behavior of granular media.

Over past decades, both continuum- and discrete-media communities have devoted great efforts to addressing this challenge. For the continuum-based approach, soil is modeled as a continuum with its mechanical response characterized by various constitutive models from the simple to the sophisticated. These models in conjunction with continuum-based numerical methods, especially Finite Element Method (FEM), can model wheel–terrain interaction (Yamashita et al., 2018; di Maria et al., 2021). However, FEM might encounter potential mesh distortion and convergence issues for large-deformation problems, e.g., considerable slippage and sinkage in the wheel–terrain context. These issues can be alleviated partially by specific techniques in sacrifice of computational efficiency and convergence (Kardani et al., 2013; Zhang et al., 2022). Therefore, mesh-free continuum methods, represented by MPM and the Smoothed-Particle Hydrodynamics (SPH), have received growing interest in tackling large deformation problems in geotechnical engineering, e.g., modeling landslides using MPM (Soga et al., 2016; Y. Zhao et al., 2023) or SPH (Nguyen et al., 2017). Meanwhile, emerging GPU-acceleration techniques have been successfully applied to tackling the massive computing (Peng et al., 2022). Recently, MPM (Agarwal et al., 2019; Xu et al., 2021) and SPH (El-Sayegh et al., 2020; Hu et al., 2021) have been introduced to model soil reactions in response to wheel motion. Nevertheless, continuum models are commonly phenomenological and, frequently fail to fully capture complicated granular behaviors (Andrade et al., 2012). This limits their application in predicting the wheel–terrain response, especially for planetary regolith.

The discrete-based approach, represented by DEM, is advantageous from the perspective that micro-mechanical behaviors can be modeled explicitly at the particulate scale; meanwhile its mesh-free nature suits modeling large deformation in the wheel–terrain interaction. Indeed, researchers have employed DEM to examine soil deformation and flow in response to the motion of rigid wheels (Johnson et al., 2015; Jiang et al., 2018; Wiberg et al., 2021) and even dust transport from the wheels (Sargeant et al., 2022) for planetary rovers, where wheels are modeled in DEM as well as soils. Moreover, wheels can be alternatively modeled in FEM and then coupled with DEM to model wheel–terrain interaction, i.e., the so-called concurrent FEM–DEM approach (Serban et al., 2019; Guo et al., 2022). Despite its advantages, DEM is computationally too expensive to solve large-scale (e.g., billions of particles and more) wheel–terrain interaction problems for future rover simulators even with the GPU acceleration (Benatti et al., 2022), while the continuum-based approach offers appreciable computational efficiency.

Recently, modeling of granular media has been attempted using a class of hierarchical multiscale approaches that leverage the strengths of both continuum- and discrete-based methods, e.g., FEM–DEM (Guo and Zhao, 2014) and MPM–DEM (Liang and Zhao, 2019). The fundamental idea is to bypass the conventional constitutive model with the DEM-simulated response of representative volume elements (RVEs). The extra computing from DEM simulations is massive but can be significantly accelerated on GPUs (Zhao et al., 2021). The hierarchical approaches have also been extended to multi-physics problems, e.g., FEM–DEM (Guo and Zhao, 2016; Zhao et al., 2020) and MPM–DEM (Zhao et al., 2022). The hierarchical approach can be a better alternative to the sole continuum or discrete-based approach for modeling of wheel–terrain interaction. Indeed, the hierarchical FEM–DEM approach has been applied to modeling tire-terrain interaction (Yamashita et al., 2019).

Nevertheless, there are three specific challenges of simulating wheel–terrain interaction for planetary rovers as follows: (1) planetary regolith particles are often sharp and angular due to scarce weathering, which may significantly influence the soil response but is not fully considered in the previous studies due to the complexity of modeling it; (2) wheel grousers make the wheel–terrain interaction even more complex; and (3) terrains such as sand-rock mixtures with extremely wide grain size distributions are often encountered by a rover yet are not considered in previous wheel–terrain interaction models.

To address these three challenges in off-road wheel–terrain interaction, we propose a multiscale framework that captures the coupled effects of discrete gravel/rock flow and continuum sand/clay deformation on wheel and rover performance. The framework integrates DEM, MPM, and a contact-coupling interface. The interface uses DEM to resolve discrete particle dynamics and MPM to model large-deformation continuum behavior, and further extends both through an arbitrary contact-coupling strategy based on Signed Distance Field (SDF) shape parsing. As a result, the framework supports wheel–rock, wheel–sand, and rock–sand interactions within a unified scene, enabling the simulation of large-scale wheel effects, small-scale granular interactions, and mixed large–small scale coupling. In addition, we provide an end-to-end GPU implementation of DEM, MPM, and contact, along with scalable acceleration techniques for realistic large-scale simulations (e.g., NASA Mars rover operations). These techniques include ray-tracing-based contact detection for DEM, sparse-memory encoding for MPM, and an optimized SDF-based conversion that reduces contact processing from all mesh vertices to a selected proxy subset within the contact solver.

This paper is structured as follows. Section 2 introduces a wheel–terrain modeling framework, detailing interactions between wheels, rocks, and sand. Section 3 validates the framework through benchmark studies. Section 4 simulates the entrapment of NASA's *Spirit* rover, while Section 5 examines the overslip behavior of *Curiosity*, demonstrating the real-world applicability of the framework. Finally, Section 6 offers concluding remarks.

2. Computational framework

The framework classifies terrain constituents by particle size into rock/gravel and sand, leading to three distinct contact-interaction strategies. Wheel–rock interactions are treated as large-large contacts. For wheel–sand interactions, we employ a computationally efficient large–small approximation. In contrast, rock–sand interactions utilize a detailed, and more computationally expensive, large–small model. This section details these strategies, demonstrating a practical trade-off between accuracy and efficiency.

2.1. SDF model

The prevailing SDF method in computer graphics is employed to model tires or wheels due to its efficacy in contact detection. As illustrated in Fig. 2, SDFs can represent both deformable tires and non-deformable rover wheels. Fig. 2(a–b) are included only to provide a general comparison with the deformation-updated SDF treatment and are not employed in the present framework, whereas Fig. 2(c–d) illustrate the fixed-reference SDF treatment adopted in this study. Wheels exhibit complex geometries, including both convex and concave regions, that extend beyond simple primitives such as spheres or cubes. This geometric complexity imposes a substantial computational burden on wheel–terrain contact simulation. While real-world tires and wheels can deform, this study focuses on planetary rovers and simplifies the model by treating the wheel as a rigid, non-deformable object. Consequently, the term wheel hereafter denotes this rigid representation, and tire deformation is not considered.

Note that the wheel model (e.g., Fig. 2(c)) is adopted from the Mars Perseverance rover (Farley et al., 2020). In this work, the wheel is represented by two proxies: (i) its original geometric model (e.g., released by NASA) and (ii) a derived SDF model generated using in-house conversion code. The geometric proxy describes the wheel using three hierarchical primitive types (vertices, edges, and triangular faces). Together with the same data structure for the rock geometry, this representation enables our high-performance ray-tracing DEM solver for wheel–rock interactions; details are provided in our Ray-Tracing DEM work (Zhao and Zhao, 2023).

The SDF is generated on a uniform orthogonal background grid whose dimensions are set to 120% of the AABB of the original geometry. The STL surface information is first mapped to the grid, followed by signed-distance propagation and correction. Cell-wise SDF values support efficient coarse queries, whereas nodal values are interpolated for local distance and contact-normal evaluation. The SDF resolution (N) is defined as the number of isotropic cells along the longest axis of the background box. As shown in Fig. 3, both the surface and volume reconstructions converge with increasing N. The simpler particle geometry converges more rapidly than the wheel, and resolutions of ($N = 40$) and ($N = 100$) are therefore adopted for the particle and wheel, respectively. The associated computational and memory requirements for these two resolutions remain manageable because each SDF template is generated only once during preprocessing and subsequently reused. Geometrically identical instances can share the same SDF template through the corresponding scaling and rotational transformations, rather than requiring an independent SDF reconstruction for each object.

2.2. Wheel–rock interaction

The motion of the wheel and rock bodies is described by the following equations of motion:

$$m_i \frac{d\boldsymbol{v}_i^p}{dt} = \sum_{j=1}^{n_i^c} \boldsymbol{F}_{ij}^c + \boldsymbol{F}_i^W + \boldsymbol{F}_i^R + \boldsymbol{F}_i^S + \boldsymbol{F}_i^g, \tag{1a}$$

$$I_i \frac{d\boldsymbol{\omega}_i}{dt} = \sum_{j=1}^{n_i^c} \boldsymbol{T}_{ij}^c + \boldsymbol{T}_i^W + \boldsymbol{T}_i^R + \boldsymbol{T}_i^S \tag{1b}$$

where $\boldsymbol{v}_i^p$ and $\boldsymbol{\omega}_i$ denote the translational and angular velocities of bodies i (wheel or rock), respectively. The contact force $\boldsymbol{F}_{ij}^c$ arises from DEM interactions between bodies i and j of the same type, with n_i^c being the number of contacts involving bodies i. Wheel–rock interactions contribute the force $\boldsymbol{F}_i^W$ for a wheel and $\boldsymbol{F}_i^R$ for a rock particle. If sand is present, an additional contact force $\boldsymbol{F}_i^S$ accounts for sand interactions. The gravitational force is $\boldsymbol{F}_i^g$. The net torque on body i includes the same-type contact contribution $\boldsymbol{T}_{ij}^c$, the wheel-induced torque $\boldsymbol{T}_i^W$, the rock-induced torque $\boldsymbol{T}_i^R$, and, when sand is included, the sand torque $\boldsymbol{T}_i^S$. The mass and moment of inertia of rock particle i are denoted by m_i and I_i, respectively.

Although a purely geometric wheel–rock representation (e.g., STL) is conceptually straightforward, it fails to scale to wheel–soil scenarios due to prohibitive computational cost. In even moderate soil domains, the number of sand particles can exceed that of rocks by a factor

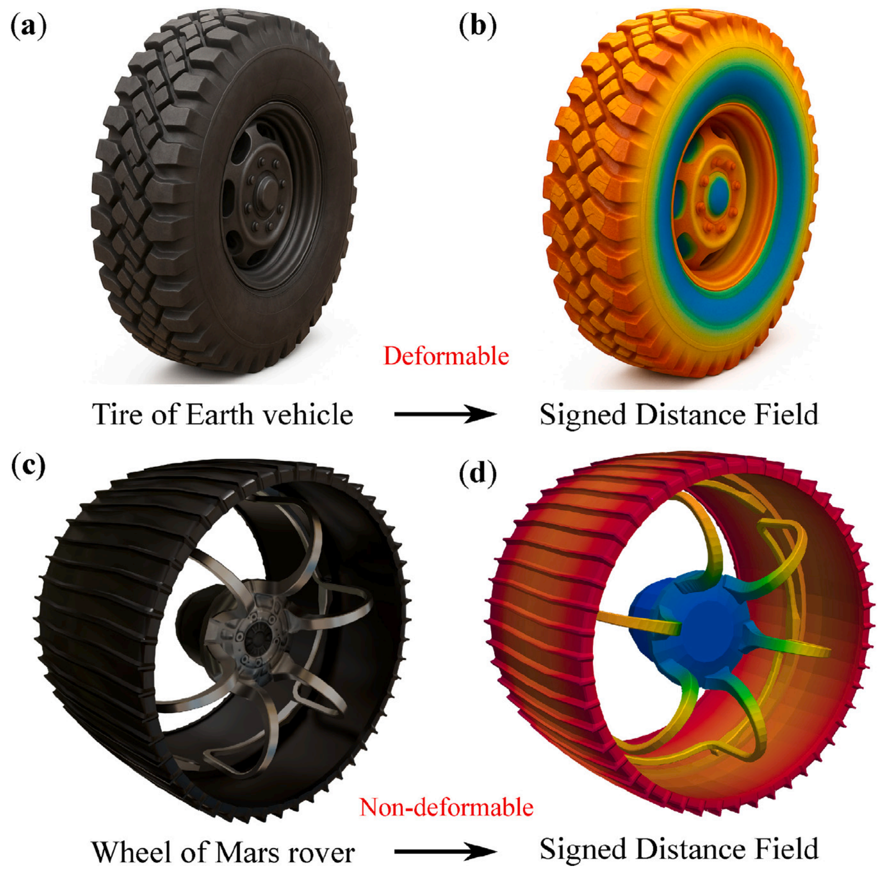

Fig. 2. Conceptual comparison of SDF representations for deformable and rigid bodies: (a) a deformable tire and (b) its deformation-updated SDF; (c) the rigid Perseverance rover wheel adopted in this study and (d) its fixed reference SDF used for wheel–terrain contact.

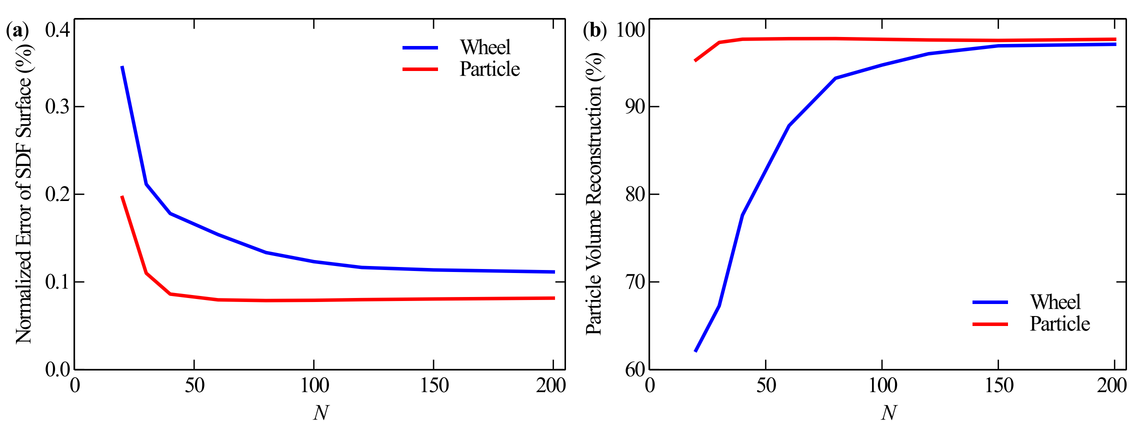

Fig. 3. Influence of SDF resolution on geometric reconstruction: (a) normalized surface reconstruction error and (b) reconstructed volume relative to the original geometry for the wheel and particle.

of 50–100. For instance, a system containing 10 000 rocks and 500 000 sand particles can produce millions of primitive-level contact pairs (e.g., vertex-triangle tests), rendering a geometry-only proxy impractical for wheel–terrain simulation. Introducing SDFs for wheel–sand and rock–sand interactions is expected to alleviate this bottleneck. The SDF approach assumes that, at the sand length scale, particle-shape effects exert only a weak influence on the contact response; hence, sand grains may be approximated as ideal spheres. With an SDF proxy for the wheel (or rock) and a spherical sand particle, contact evaluation reduces to a single query: the penetration depth equals $r-\phi(\mathbf{x})$, where $\phi(\mathbf{x})$ is the SDF value at the particle center $\mathbf{x}$ and r is the particle radius; the contact normal is given by $\nabla\phi(\mathbf{x})$. To account for variations in sand length scales, we employ a locally refined SDF-based proxy. Each sand sphere is augmented with a small set of vertex samples (e.g., no more than nine, arranged in a 3×3 grid over the potential contact patch). Contact quantities at each vertex are combined (e.g., averaged) to yield the final contact response. This local refinement maintains computational efficiency while enhancing resolution and accuracy.

To efficiently manage computational resources for wheels and rocks, we avoid generating separate representations for each object that shares the same geometry, even when instances differ only in scale or rotation. Instead, particle shapes are grouped into a set of templates, each defined in a normalized reference configuration and mapped to specific instances via scaling and rotation. Thus, each SDF template is computed only once prior to simulation. During each time step, regardless of the solver used, we can transform a query point back to the reference SDF coordinates via inverse scaling and rotation. For example, if all wheels (e.g., six) share the same geometry, only one SDF template is required. Similarly, for terrains with numerous rocks of recurring shapes, a small library of SDF templates enables economical simulation while still supporting rover performance prediction.

2.3. Wheel–sand interaction

2.3.1. Governing equations

The wheel–sand interaction framework extends an MPM-based sand solver (Chen et al., 2025) by incorporating a contact interface that computes the contact response. Accounting for contact forces exerted on the sand, the governing equations read:

$$\frac{D\rho}{Dt} = 0 \tag{2a}$$

$$\rho \boldsymbol{a} = \nabla \cdot \boldsymbol{\sigma} + \boldsymbol{F}^b \tag{2b}$$

$$\boldsymbol{F}^b = \rho \boldsymbol{g} + \boldsymbol{F}^W + \boldsymbol{F}^R \tag{2c}$$

where $\boldsymbol{a}$ is the acceleration, $\boldsymbol{\sigma}$ the Cauchy stress tensor, and ρ the mass density. The body-force term $\boldsymbol{F}^b$ includes gravitational loading $\rho \boldsymbol{g}$ as well as contact contributions from the wheel $\boldsymbol{F}^W$ and the rock $\boldsymbol{F}^R$. Multiplying Eq. (2) by the weighting function $\delta \boldsymbol{u}$ gives the weak form of momentum balance:

$$\int_{\Omega} \rho \boldsymbol{a} \cdot \delta \boldsymbol{u} dV = \int_{\Omega} \boldsymbol{F}^b \cdot \delta \boldsymbol{u} dV + \int_{\partial\Omega} \boldsymbol{\tau} \cdot \delta \boldsymbol{u} dS - \int_{\Omega} \boldsymbol{\sigma} \cdot \nabla \delta \boldsymbol{u} dV \tag{3}$$

where Ω is the solution domain and $\partial\Omega$ its boundary. The surface traction $\boldsymbol{\tau} = \boldsymbol{\sigma} \cdot \boldsymbol{n}$ acts on the domain boundary, with $\boldsymbol{n}$ denoting the outward unit normal vector in the current configuration.

Applying dual interpolation to the weak form of the momentum balance gives the discrete MPM formulation for the nodal mass and momentum:

$$m_i^{(n)} = \sum_p m_p^{(n)} S_{ip}^{(n)} \tag{4a}$$

$$\boldsymbol{p}_i^{(n)} = \sum_p \boldsymbol{p}_p^{(n)} S_{ip}^{(n)} \tag{4b}$$

where the material-point momentum $\boldsymbol{p}_p$ is extrapolated to the background grid using the material-point mass m_p and the grid shape function S_{ip}.

The momentum at each background-grid node is then advanced in time according to the total nodal force $\boldsymbol{f}_i$:

$$\boldsymbol{p}_i^{(n+1)} = \boldsymbol{p}_i^{(n)} + \boldsymbol{f}_i^{(n)} \Delta t. \tag{5}$$

The total nodal force is composed of external and internal contributions, denoted by $\boldsymbol{f}_{i,\mathrm{ext}}$ and $\boldsymbol{f}_{i,\mathrm{int}}$, respectively:

$$\boldsymbol{f}_{i,\mathrm{ext}}^{(n)} = \sum_p \boldsymbol{F}_p^{b,(n)} S_{ip}^{(n)} + \int_{\partial\Omega_\tau} \boldsymbol{\tau} S_i^{(n)} \, dA, \tag{6a}$$

$$\boldsymbol{f}_{i,\mathrm{int}}^{(n)} = -\sum_p V_p^{(n)} \boldsymbol{\sigma}_p^{(n)} \cdot \nabla S_{ip}^{(n)}. \tag{6b}$$

where $\boldsymbol{F}_p^b$ and $\boldsymbol{\tau}$ denote the body force and boundary surface traction, respectively, and $\boldsymbol{\sigma}_p$ is the stress at material point p, interpolated using the gradient of the shape function $\nabla S_{ip}^{(n)}$.

2.3.2. Contact detection and force enforcement

The wheel–sand contact algorithm employs a triple-cached strategy (Fig. 4) combined with an MPM contact substepping scheme. For a single wheel, the three caches are organized hierarchically: (**a**) a periodically updated neighbor list (cyan), (**b**) an axis-aligned bounding box (AABB) test for the wheel, and (**c**) an SDF query. Contact resolution is substepped because contact constraints operate at a finer length scale than the MPM update; consequently, contact iterations generally use a smaller timestep than the MPM. Unless otherwise noted, we use 100 contact substeps per MPM step. Within each MPM step, the first cache is evaluated by constructing a wheel neighbor list (solid-blue material points inside the cyan rectangle in Fig. 4), which remains fixed during the subsequent contact substeps (e.g., the next 100 contact steps). The remaining caches operate solely on this neighbor list to improve efficiency.

The second cache performs an AABB check: only neighbor-list members inside the wheel AABB (solid/dashed hollow disks) are passed to the third cache for an SDF test. A 2D slice of the 3D SDF illustrates that the wheel surface can include both convex and concave features and may exhibit ring-like geometry; consequently, two zero-level isosurfaces may appear in the 2D SDF. A material point is considered in contact when its SDF value is less than the sand particle radius (taken as the average material-point semi-domain; see Chen et al. (2023)); such points are indicated by solid and hollow disks. Because of this two-isosurface structure, candidate contact points may lie on either the outer wheel surface or the rim surface.

For each contact point, additional SDF data is required to compute the contact normal. The SDF is stored on a structured grid surrounding the wheel. For a contacting material point, we identify its parent grid cell, gather the SDF gradients at the eight cell vertices, and compute their interpolated average to obtain the contact normal $\boldsymbol{n}$. This study employs linear interpolation for this averaging, though higher-order schemes can be incorporated straightforwardly. The Hertz–Mindlin contact model is employed to solve contact force. The normal contact force is given by

$$\boldsymbol{F}_n = \frac{4}{3} E^* \sqrt{R^*} \delta_n^{3/2} \boldsymbol{n} \tag{7}$$

where $\boldsymbol{n}$ is the contact normal and δ_n is the normal penetration. The equivalent Young's modulus E^* and equivalent radius R^* are defined as

$$\frac{1}{E^*} = \frac{1-\nu_W^2}{E_W} + \frac{1-\nu_S^2}{E_S} \tag{8a}$$

$$\frac{1}{R^*} = \frac{1}{R_W} + \frac{1}{R_S} \tag{8b}$$

where E_W and E_S denote the Young's moduli of the wheel and soil, respectively, and ν_W and ν_S are their corresponding Poisson's ratios. The tangential contact force is updated incrementally according to

$$\Delta \boldsymbol{F}_t = 8G^* \sqrt{R^* \delta_n} \Delta \boldsymbol{\delta}_t \tag{9a}$$

$$\frac{1}{G^*} = \frac{2-\nu_W}{G_W} + \frac{2-\nu_S}{G_S} \tag{9b}$$

where $\Delta \boldsymbol{\delta}_t$ is the incremental tangential displacement over the current time step. The equivalent shear modulus G^* is obtained from the shear moduli and Poisson's ratios of the wheel and soil. The tangential force is bounded by the Coulomb sliding friction, i.e.,

$$|\boldsymbol{F}_t| \leqslant \mu |\boldsymbol{F}_n| \tag{10}$$

where μ is the coefficient of friction.

Because the tangential contact force is history dependent, state variables such as the accumulated tangential displacement must be tracked for each active contact. This requirement is especially important in the present wheel–soil system, where the large scale separation between the wheel and the sand particles results in contact and neighbor lists that are large yet sparse. In addition, the set of particles in contact with the wheel can change from one time step to the next. Consequently, storing contact states in a contiguous linear data structure provides limited benefit. We therefore adopt a hash-based indexing scheme in which each sand material point maps its particle index to a contact index. This approach enables efficient retrieval of the corresponding contact state, supports single-operation reads, and facilitates the inter-step transfer of history variables, including the previous contact normal and the accumulated tangential displacement.

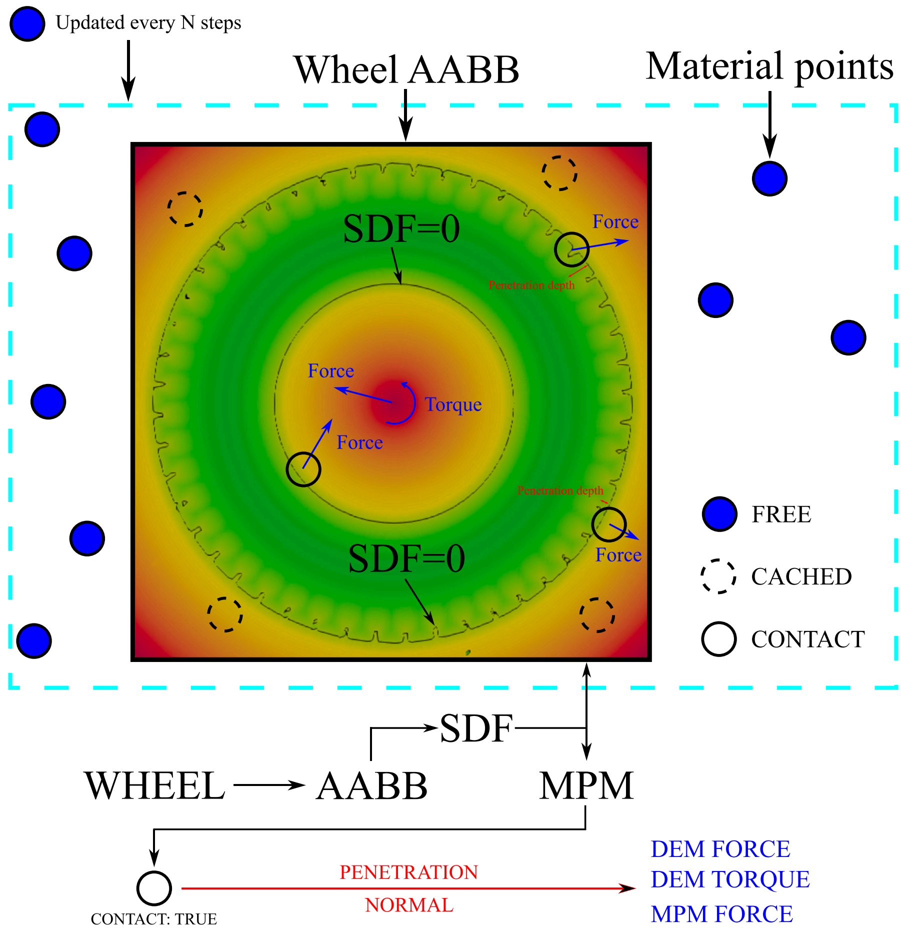

Fig. 4. Triple-cached algorithm for wheel–sand interaction. The dashed cyan buffer region periodically captures candidate material points, and an AABB performs further filtering. The remaining contact candidates are evaluated using the SDF, and the resulting contact information is passed to the contact law to compute the corresponding forces and torque.

Owing to the pronounced scale separation between the wheel and the sand discretization, rotational effects on individual sand material points are neglected. This approximation is justified because the characteristic branch vector associated with a sand material point is much smaller than that associated with the wheel; hence, the torque induced on the sand-side discretization is negligible. The interaction model therefore retains the force and torque exerted by the sand on the wheel, together with the equal-and-opposite contact force exerted by the wheel on the sand. At each contact substep, the impulse is applied directly within the wheel DEM solver. The corresponding sand-side impulses are accumulated over all substeps and returned as a time-averaged impulse after the substepping procedure is complete.

2.4. Rock–sand interaction

Unlike the wheel–sand interaction described in Section 2.3, rock–sand interactions incur substantially higher computational overhead. This overhead arises because the number of rock and sand particles can be large, and when sampled over an extended domain, the cost increases further. Consequently, computational efficiency is as important as accuracy. One might ask why the sand material points are not simply passed to the DEM engine so that DEM alone handles the wheel–rock–sand interaction. Although feasible, this approach would at least double the memory footprint, since the same state would need to be stored in both DEM and MPM. Moreover, as noted in Section 2.2, an optimized SDF proxy can also reduce contact costs, making a pure DEM solver less necessary.

The rock particle shape used in this study, illustrated by a representative two-dimensional slice in Fig. 5, was generated from a CT-scanned STL geometry and scaled to a major-axis length of approximately 20 mm. The resulting particle has a sphericity of about 0.90, a minor-to-major axis aspect ratio of about 0.55, and a solidity of about 0.98. These geometric characteristics are broadly comparable to those of the Type 7 Martian clasts reported by Khan et al. (2022) for the Gale Crater site explored by *Curiosity*, for which the measured aspect ratio, sphericity, solidity, and major-axis length are approximately 0.54–0.84, 0.70–0.86, 0.89–0.97, and 20–23 mm, respectively. Thus, the adopted STL particle is not intended to replicate a specific Martian rock, but rather to represent a sub-angular clast morphology intermediate between highly angular and well-rounded shapes. This choice allows the simulations to account for the non-spherical contact geometry of individually resolved Martian surface rocks while retaining a controlled particle morphology for the wheel–rock–sand interaction analysis.

Fig. 5 summarizes the workflow for detecting rock–sand contacts. We adopt the triple-cache strategy previously used for wheel–sand interactions, but revise it into a ghost-cell-based, AABB- and SDF-assisted formulation. This modification addresses the heterogeneity of contact density over large domains containing both rocks and sand: some regions exhibit a high density of rock–sand contacts, whereas others contain none. In densely interacting regions, constructing a separate neighbor list for each rock, as in the wheel-based approach, leads to substantial redundant computation and memory usage. Instead, we partition the domain into ghost cells, and all rocks within a subdomain share a single candidate sand-particle list. This shared list

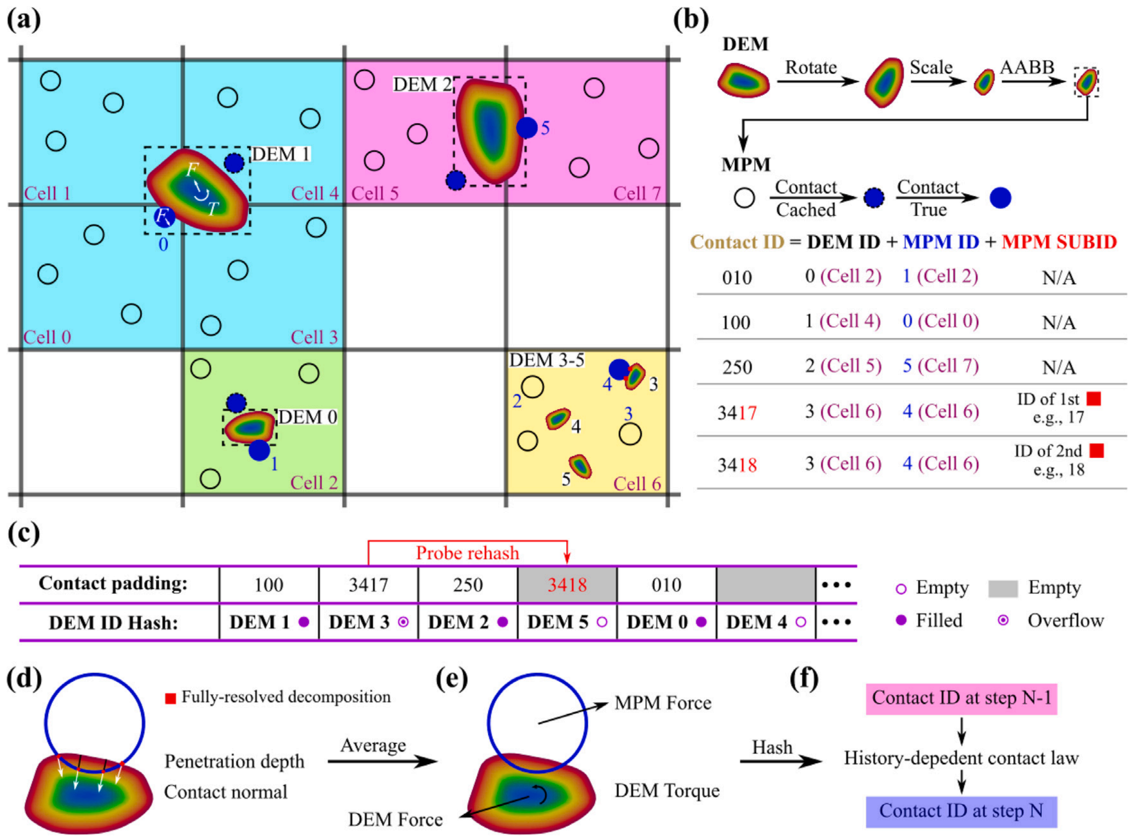

Fig. 5. Workflow of the rock–sand contact algorithm: (a) Ghost contact cells, together with the AABB and SDF, provide multi-stage material-point filtering; (b) Contact pairs are encoded into a 1D identifier to enable hashing into a scatter-style contact padding; (c) Contact allocation accommodates rocks of different sizes and coordination numbers; and (d-f) The vertex-based contact law between rock and sand particles.

enables efficient culling of potential contacts while avoiding duplicated neighbor-list construction.

The ghost-cell domain is determined by the MPM solver rather than prescribed arbitrarily. In our MPM implementation, spatially adjacent sand material points are densely packed and organized into *pages*. Each page is an abstract memory block that stores material points located within a small contiguous region of the background grid, for example, neighboring 4 × 4 × 4 cells in three dimensions. Material points assigned to the same page are stored consecutively in memory, and each page occupies a fixed memory block of 4096 KB. This page-based data layout improves memory locality and cache reuse during particle-to-grid and grid-to-particle interpolation, thereby enhancing the computational efficiency of the MPM solver.

Given any sand particle index, we can efficiently retrieve its page index as well as the start and end indices of the material points in that page. These mappings are already constructed and maintained by the MPM solver for its iterations, and thus can be reused here without additional computation. Accordingly, the contact ghost-cell domain spans $N_x p_x \times N_y p_y \times N_z p_z$, where N_* denotes the number of MPM pages spanned along each axis and p_* the page spacing. By spanning at least one MPM page, the ghost-cell domain directly benefits from the sparse memory layout used in MPM, improving computational efficiency. With this organization, at each MPM step, rocks query their parent ghost cells in parallel to obtain the neighboring sand pages. The resulting page indices are then frozen for the subsequent contact substeps, analogous to a neighbor list in wheel–sand interaction.

During each substep, a rock iterates over all material points in the selected pages and filters contact candidates using its AABB and SDF evaluations. Because the sand is modeled as an MPM continuum, the radius used for a sand material point is not a physical grain radius but an effective contact/support radius. For a grid cell size Δx and N_{mpc} material points per cell, one material point represents a volume $V_p = \Delta x^3 / N_{\mathrm{mpc}}$, and its effective radius is defined as

$$r_p = \eta \left(\frac{3V_p}{4\pi} \right)^{1/3} \tag{11}$$

where η controls the contact support size and is set to unity in this study. In Fig. 5, DEM rocks 0, 1, and 2 identify 1, 0, and 5 contacting sand material points, respectively. This strategy is effective when rock and sand material-point sizes are well separated, but becomes less robust when a rock is comparable in size to the effective material-point radius, as illustrated by DEM 3. In this regime, we introduce an additional SDF-based optimization: marked vertices on the potential contact patch provide a more detailed contact description and better capture shape effects. For example, vertices 17 and 18 of DEM 3 are activated, refining the contact state on sand material point 4 and yielding two contacts for a single rock–sand pair.

The substantially larger number of contacts in rock–sand systems necessitates a different strategy for recording contact states and tracking history variables across time steps. As shown in Fig. 5(b), the contact pairs in subfigure (a) are first encoded into a unique 1D identifier by concatenating the DEM index, the MPM index, and a vertex sub-ID (0 if unavailable, otherwise a 1-based vertex index). These 1D identifiers are then recorded in parallel into a hash padding array (as in the wheel–sand case). However, the larger data volume increases the likelihood of race conditions during insertion. To mitigate this, we apply a mixing function to the 1D identifiers prior to registration, followed by a probe-hashing stage.

As shown in subfigure (c), the hash layout enhances locality by mapping contacts arising from spatially proximate rock–sand interactions to the same memory page. As a result, identifiers 3417 and 3418 collide in the same bin (the second bin), whereas many other contacts occupy a single slot or leave their slots unused. These three cases correspond to the *overflow*, *filled*, and *empty* states, respectively. Because each slot can store at most one contact, resolving *overflow* is the primary concern. In the example, DEM 4 and DEM 5 have no contacts and thus remain *empty*. Furthermore, since DEM 5 is closer to DEM 3 than DEM 4, DEM 5 contributes its bin to DEM 3 as auxiliary storage. This approach balances the use of hash padding by reassigning overflowing entries to empty bins, avoiding global over-allocation while preserving a compact memory layout. After probe hashing resolves collisions, only *filled* (1) and *empty* (0) states remain. A prefix sum over these states assigns each filled slot a dense index, which is then used to evaluate the contact law efficiently.

The contact law, illustrated in subfigures (d–f), accounts for both SDF vertex-proxy averaging and history-variable tracking. Its normal component follows the same Hertz–Mindlin formulation used for wheel–sand interaction. Fully resolved DEM–MPM contact treatments can provide detailed descriptions of comparable-size particle interactions (Ren et al., 2022, 2023), but applying such treatments to every rock–sand contact would introduce substantial computational overhead in large-scale systems. In realistic rock–sand terrain, the resolved DEM rocks are generally much larger than the effective contact radius of the MPM sand material points. Consequently, a rock surface is typically represented by multiple neighboring material points, and a single SDF-based contact point for each rock–material-point pair provides a reasonable approximation for most interactions. We therefore retain this efficient treatment as the default while introducing sparse vertex sampling when the characteristic sizes of the DEM rock and MPM material point become comparable. In this regime, a single contact point may insufficiently resolve the local interaction, particularly for irregular or locally concave DEM surfaces. A sparse set of vertices is therefore sampled over the potential MPM contact region, as illustrated by the marked vertices in subfigure (d). Although shown in two dimensions for clarity, the vertex sampling is performed in three dimensions. Each vertex independently probes the DEM SDF and may form an individual contact pair with its own contact normal and penetration depth. When multiple vertices participate in the same interaction, their contributions are averaged. For history tracking, each contact retrieves its previous state by hashing the triplet (DEM index, MPM index, vertex sub-ID) and using the associated dense index obtained from the prefix-sum result. Thus, although the proposed treatment is not intended to constitute a fully resolved DEM–MPM contact formulation, it balances accuracy and efficiency by providing additional geometric resolution for comparable-size interactions that would otherwise remain under-resolved.

The present contact treatment is designed to provide an energy-consistent geometric definition of contact by introducing potential-based models as proposed in the literature (Feng, 2021a,b). For wheel–rock and rock–rock interactions resolved by the DEM solver, our previous study demonstrated the energy-conserving behavior of the adopted contact formulation in the ideal elastic limit (Zhao and Zhao, 2023). For wheel–sand and rock–sand interactions, the SDF representation avoids the independent prescription of penetration depth and contact normal. Instead, the penetration is evaluated from the signed-distance value, while the normal direction is obtained from the normalized gradient of the same scalar field. This construction is consistent with the central principle of energy-conserving contact theories for arbitrarily shaped particles, in which the contact geometry and normal force are derived from a common scalar potential. In the present implementation, the SDF serves as this geometric potential for defining the local contact kinematics, after which the Hertz–Mindlin law is applied as a penalty-type contact response. Nevertheless, strict global energy conservation is not expected in the complete wheel–rock–sand simulation. Friction and damping deliberately dissipate energy, whereas the prescribed wheel motion can inject mechanical energy into the system. Moreover, the staggered DEM–MPM coupling and the MPM particle-grid projection may introduce additional numerical dissipation. These effects are consistent with the strongly dissipative nature of rover-terrain interaction. Thus, the objective of the present framework is to maintain a consistent derivation of contact forces and stable momentum exchange, rather than to enforce exact conservation of the total discrete mechanical energy.

Note that the present study deliberately adopts a single rigid-wheel configuration, as its primary objective is to establish and evaluate the proposed multiscale wheel–terrain interaction framework rather than to reproduce the full dynamics of a specific rover. At the wheel-subsystem level, the prescribed wheel load and actuation conditions represent the operating state of an individual rover wheel, while the computed terrain reaction forces and torques provide the interface quantities required for integration with a full vehicle-dynamics model. This idealization is particularly appropriate for planetary rovers, which typically operate at low translational and rotational velocities; under such conditions, vehicle-scale inertial effects and rapid suspension or drivetrain transients are less dominant than in conventional high-speed terrestrial vehicles. In addition, the metallic rover wheels considered here are substantially stiffer than the surrounding rock-soil terrain, which supports their treatment as rigid bodies when the primary focus is terrain deformation and wheel–terrain contact. The current configuration therefore resolves local wheel sinkage and translation, together with the time-dependent normal and tangential reactions and driving torque. However, because the wheel is not connected to a chassis or suspension system, the model does not capture inter-wheel load redistribution, suspension-induced variations in individual wheel loads, or rover pitch and roll during severe asymmetric sinkage. Capturing these vehicle-level responses would require coupling the present framework with a multibody rover model, which will be addressed in future work.

2.5. Workflow of the wheel–rock–sand contact framework

Fig. 6 presents a flowchart of the wheel–rock–sand framework. The top-level components are an MPM solver and a substepped contact solver, with MPM acting as the caller and the contact solver as the callee. At the start of the simulation, wheel and rock properties are initialized from STL inputs, precomputed into SDFs, and passed to the MPM coupling interface, while the sand is initialized directly as MPM material-point data. The MPM solver configures numerical parameters (e.g., time step, substep ratio, and sand constitutive model) and provides the contact solver with interface parameters such as contact stiffness and friction.

From time step n to $n + 1$, the MPM solver first reorders the sand material points into a spatially compact memory layout to improve cache locality. An initial contact-cache update is then performed for the MPM–DEM interactions between sand and the DEM wheel/rocks. For each DEM particle, candidate sand material points are identified using its reference SDF together with its current rotation and scaling. Specifically, the sand material points are mapped into the local coordinate system of each wheel or rock by applying the inverse of the corresponding transformation, after which the fixed reference SDF is queried to determine potential contacts in the broad-phase search.

The contact solver is then executed during the substepping stage. The wheel–sand and rock–sand contact engines are applied sequentially to compute the contact forces and torques acting on the potential contacts of wheel, rocks, and sand. The DEM solver also resolves wheel–rock contact and advances the wheel and rock states through Newton integration, subject to the prescribed boundary conditions. Meanwhile, the corresponding reaction forces on the sand material points are accumulated. At the end of the substeps, these sand forces are averaged and returned to the MPM solver. The material points then retrieve the contact forces, and the standard MPM update is performed, including particle-to-grid (P2G) transfer, grid-based Newton integration, and grid-to-particle (G2P) transfer. The procedure then advances to the next time step.

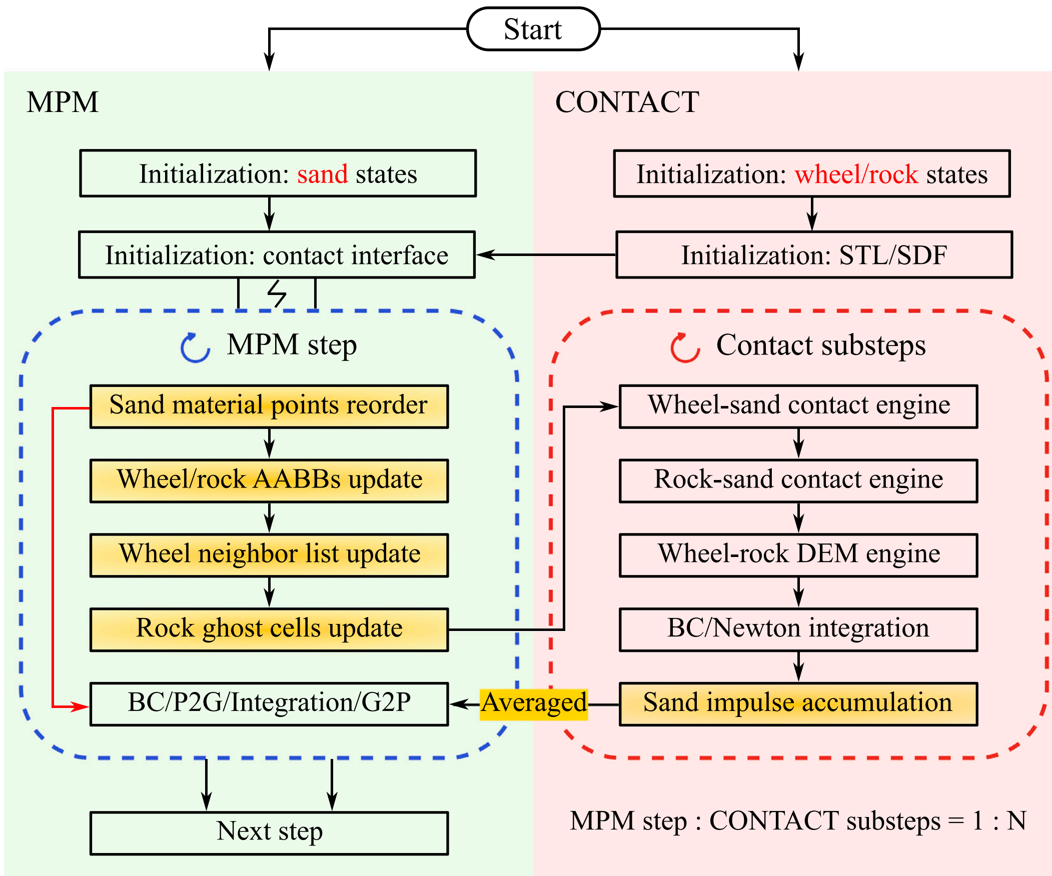

Fig. 6. Schematic of the substepped wheel–rock–sand contact algorithm within the MPM iteration. Yellow boxes denote operations that exchange information between the MPM solver and the contact solver. Unless otherwise stated, a substepping ratio of $N = 100$ is used throughout this manuscript.

3. Benchmarks

This section benchmarks the contact solver for wheel–rock, wheel–sand, and wheel–rock–sand interactions. The evaluation combines quantitative benchmarks, including analytical comparison for the head-on collision and controlled wheel-drop and rolling tests, with mechanism-oriented case studies. Together, these tests assess both the quantitative accuracy of the contact formulation and its ability to reproduce complex rover-terrain interaction mechanisms. On this basis, two NASA Mars rover incidents are further investigated. The *Spirit* case serves as both a quantitatively supported and mechanism-oriented reconstruction, because its material properties are drawn from the published literature and its results are compared with those of previous studies. By contrast, the *Curiosity* case is treated primarily as a mechanism-oriented reconstruction, owing to the lack of comprehensively calibrated, site-specific terrain properties. Dedicated benchmarks for the standalone MPM and DEM solvers are omitted here for brevity; interested readers are referred to our previous work (Zhao and Zhao, 2023; Chen et al., 2025). All benchmark simulations were performed on a system equipped with an Intel Xeon Gold 6248R CPU and an NVIDIA GeForce RTX 4090 GPU using CUDA 12.0.

3.1. Head-on collision of two spheres

The validation assesses SDF-based interactions between a DEM particle and MPM material points by simulating the collision of two spheres approaching each other (Fig. 7(a)). The left sphere is a DEM rock particle with radius 0.2 m, described by the analytical SDF $\phi(\boldsymbol{x}) = \|\boldsymbol{x} - \boldsymbol{x}_0\| - R$, $\boldsymbol{x} \in \mathbb{R}^3$ where $\boldsymbol{x}_0$ denotes the sphere center and R denotes the sphere radius. The sphere on the right represents an ideal elastic continuum discretized by MPM material points. Although MPM is later used to model sand terrain, this sphere is introduced here solely to benchmark the DEM–MPM coupling and is not intended to capture the dissipative behavior of real sand. It has the same radius as the DEM sphere and is initially positioned 0.5 m away. Two MPM resolutions are considered, with particles per cell (PPC) of 1 and 3, yielding 33 552 and 904 960 material points, respectively, on an MPM grid with spacing 0.01 m. The simulation is initialized by prescribing velocities of 1 m/s for the DEM sphere and −1 m/s for the MPM sphere. Both bodies share identical material properties: density $\rho = 2\,000$ kg/m^3, Young's modulus $E = 1 \times 10^7$ Pa, and Poisson's ratio $\nu = 0.3$. The total simulated time is 0.1 s with a time step of 1×10^{-6} s. Note that for the high-resolution simulation, comprising 904 960 MPM material points, the entire simulation was completed in 196 s of wall-clock time, corresponding to a computational rate of 510 time steps per second. Fig. 7(b) compares the velocity histories of the DEM and MPM spheres and demonstrates the expected exchange of velocities during the collision.

Fig. 8(a) shows the energy evolution of the two-sphere system. The total energy, E_{tot}, comprises the kinetic energies of the DEM sphere and the MPM particles,

$$E_{k,\text{DEM}} = \frac{1}{2} m_{\text{DEM}} \|\boldsymbol{v}_{\text{DEM}}\|^2 \tag{12a}$$

$$E_{k,\text{MPM}} = \frac{1}{2} \sum_p m_p \|\boldsymbol{v}_p\|^2 \tag{12b}$$

where m_{DEM} and m_p denote the masses of the DEM sphere and the MPM particle p, respectively, and $\boldsymbol{v}_{\text{DEM}}$ and $\boldsymbol{v}_p$ are their corresponding velocities.

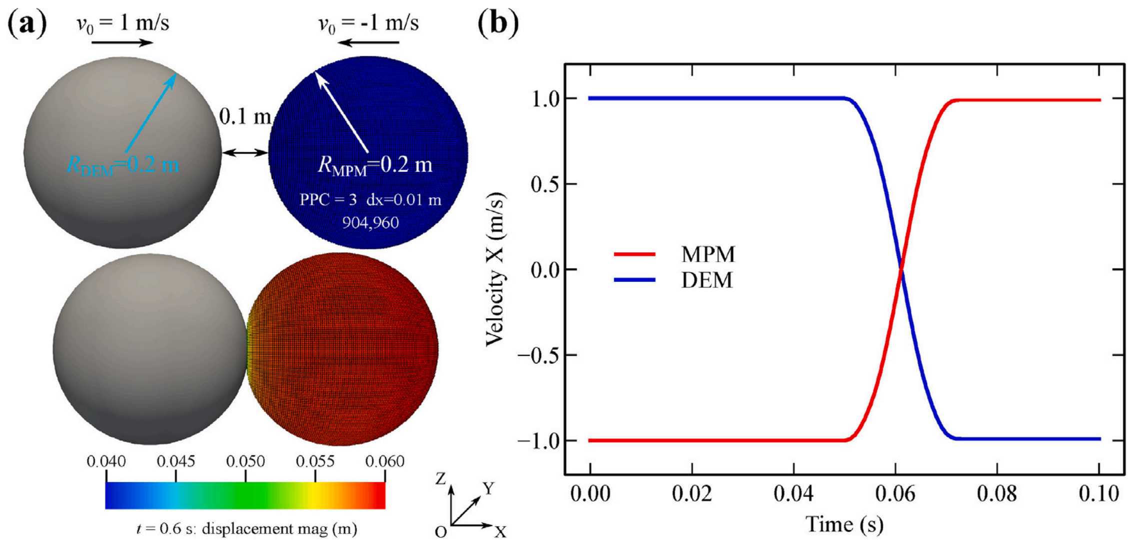

Fig. 7. Head-on collision between a DEM sphere (left) and an MPM sphere (right): (a) Snapshots; (b) Evolution of the horizontal velocities of both spheres.

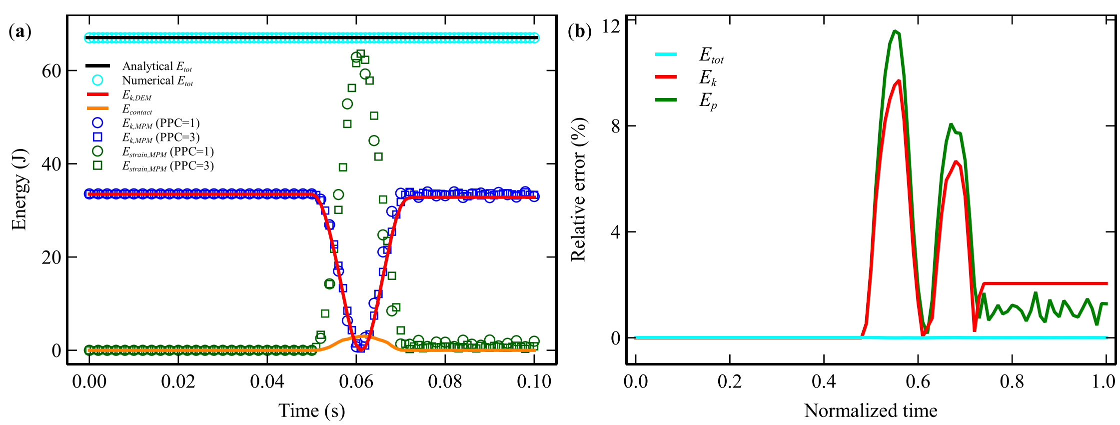

Fig. 8. Energy evolution and analytical comparison for the head-on collision: (a) time histories of the energy components of the DEM and MPM spheres for PPC = 1 and 3, corresponding to 33 552 and 904 960 MPM material points, respectively; and (b) relative errors in the total energy, DEM-sphere kinetic energy, and potential energy with respect to the analytical Hertz–Mindlin solution.

The total energy further includes the MPM strain energy, E_{strain}, and the MPM–DEM contact potential energy, E_{contact}, defined as

$$E_{\text{strain}} = \frac{1}{2}\sum_{p} \boldsymbol{\sigma}_p : \boldsymbol{\epsilon}_p \tag{13a}$$

$$E_{\text{contact}} = \frac{1}{2}k_n\delta^2 \tag{13b}$$

where $\boldsymbol{\sigma}_p$ and $\boldsymbol{\epsilon}_p$ are the stress and strain tensors at material point p, respectively, k_n is the DEM normal contact stiffness, and δ is the contact penetration.

The results show that the total energy (cyan markers) closely matches the analytical value computed from the initial configuration (i.e., the total kinematics of the two spheres). After contact occurs, the DEM and MPM kinetic energy is transferred into contact energy and MPM strain energy. As the collision progresses toward its final stage, kinetic energy is gradually recovered from the contact energy. For DEM, the kinetic energy is fully recovered; for the material points, because zero damping is imposed, a sinusoidal and staggered strain-kinetic energy exchange persists. This effect is most pronounced for PPC = 1 (sphere markers). As the material-point resolution increases (PPC = 3, square markers), the strain and kinematic oscillations are significantly reduced, indicating convergence toward the analytical solution once a sufficient resolution threshold is reached.

According to Hertz–Mindlin contact theory, the normal contact force is expressed as,

$$\boldsymbol{F}_n = \frac{4}{3}E^*\sqrt{R^*}\delta^{\frac{3}{2}}\boldsymbol{n} \tag{14}$$

where E^* and R^* denote the equivalent Young's modulus and equivalent radius, respectively.

Based on this formulation, analytical histories of the total, kinetic, and elastic potential energies can be derived. For comparison with the coupled simulation, the elastic potential energy comprises the contact potential energy and the strain energy stored in the MPM sphere. The relative errors of the present numerical results with respect to the analytical Hertz–Mindlin predictions are presented in Fig. 8(b). The total-energy error remains negligible throughout the collision, whereas the kinetic- and potential-energy errors reach approximately 10% during the rapid transition from initial contact to maximum compression, at which the relative velocity momentarily vanishes. These localized discrepancies are attributed primarily to the quasi-static assumptions underlying classical Hertz theory, which represent elastic deformation through the instantaneous contact indentation but do not explicitly resolve the transient stress–strain evolution and elastic-wave propagation captured by the MPM sphere during dynamic collision.

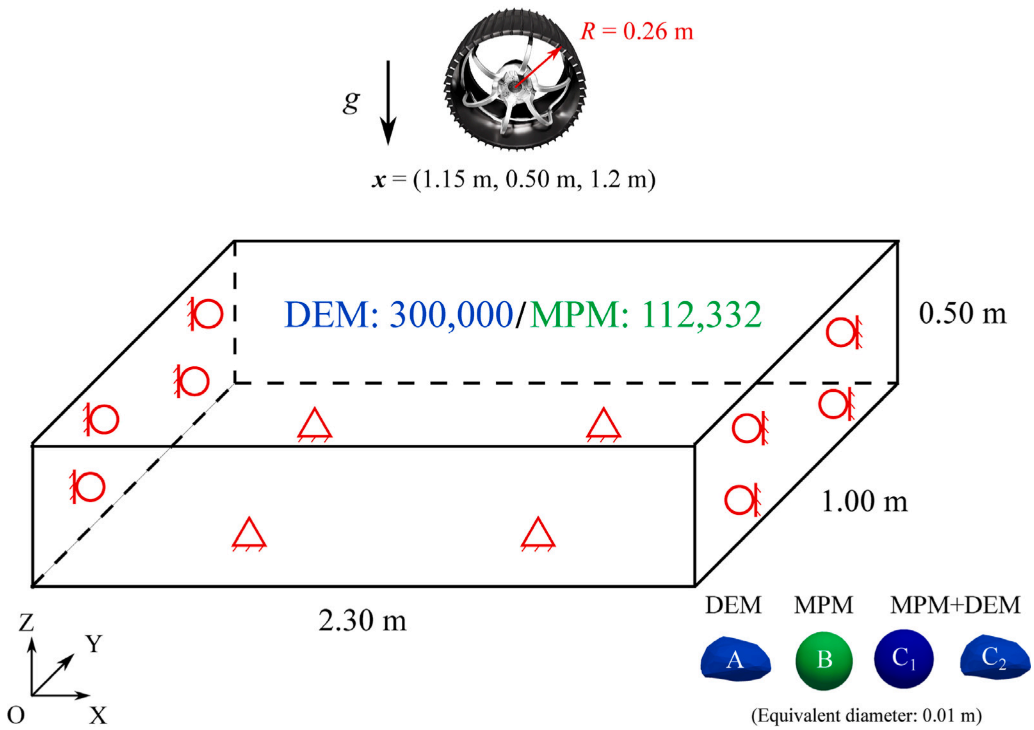

Fig. 9. Terrain configurations used in the wheel-drop tests: (a) Pure DEM rock terrain (300 000 particles), (b) Pure MPM sand terrain (112 332 material points), and (c) Mixed rock–sand terrain (8000 DEM particles and 62 360 MPM material points).

3.2. Free-fall wheel drop on a rock/sand terrain

The NASA Perseverance wheel STL model (nominal radius $\approx$ 0.26 m; volume 0.0058 m^3) is used to simulate a single-wheel free-fall drop onto three terrain types: rock, sand, and mixed rock–sand, measuring $2.3\ \text{m} \times 1.0\ \text{m} \times 0.5\ \text{m}$ (Fig. 9). The rock terrain is represented entirely using DEM particles of shape A (Fig. 9), a strongly non-spherical particle with equivalent diameter 0.01 m. The sand terrain is modeled exclusively with MPM using a grid cell size of 0.01 m and PPC = 1. Accordingly, the DEM configuration contains 300 000 particles, while the MPM configuration contains 112 332 material points. The third terrain option is a mixed rock–sand configuration in which randomly selected material points are removed and replaced by DEM particles. Because the bounding box of the irregular DEM shape is slightly larger than an MPM cell, a $2 \times 2 \times 2$ block of cells is exchanged for one DEM particle. This mixed terrain comprises 8000 DEM particles and 62 360 remaining material points.

The terrain is initialized in a gravity-free state and then subjected to a geostatic settling stage under gravity. A damping coefficient of 0.3 is applied to promote convergence to equilibrium. After equilibrium is reached, the wheel is released from a height of 0.7 m above the highest point of the terrain surface to initiate free fall ($g = 9.8\ \text{m/s}^2$). The total simulation time is set to 2.5 s to ensure that the wheel reaches a near-static state on the terrain (velocity magnitude below 1×10^{-7} m/s). The time step is 4×10^{-5} s. Regarding the computational efficiency, the coupled MPM–DEM simulation, consisting of 8000 DEM particles and 62 360 material points, required 353 s of wall-clock time, achieved a computational rate of 170 steps/s, and used 1944 MB of memory. By comparison, the pure MPM simulation, with 112 332 material points, completed in 181 s at 331 steps/s and used 1906 MB of memory. The pure DEM simulation, comprising 300 000 particles, required 272 s, achieved 220 steps/s, and consumed 2862 MB of memory.

During the simulation, the lateral boundaries are constrained in the normal direction while remaining free in the Z-direction, and the bottom boundary is fully fixed. The wheel density is set to $\rho_W = 2700$ kg/m^3, corresponding to a weight of 0.153 kN ($g = 9.8\ \text{m/s}^2$). The friction coefficient between the wheel and terrain (rock and sand) is set to zero. Both rock and sand have density $\rho = 2650\ \text{kg/m}^3$. For sand, an elasto-plastic Mohr–Coulomb model is adopted with Young's modulus $E = 1 \times 10^6$ Pa and Poisson's ratio $\nu = 0.3$, friction angle $\phi = 35°$, and dilation angle $\psi = 5°$.

The terrain displacement fields at the end of the simulation are shown in Fig. 10(a–c). Under the same wheel self-weight, the sand terrain undergoes the smallest deformation, the mixed rock–sand terrain exhibits a larger deformation, and the pure rock terrain shows the largest deformation. This trend can be explained by differences in the effective wheel–terrain contact area and the associated load-transfer length scale (Zhang et al., 2026). In the MPM sand case, the wheel load is transmitted through a continuum-like material-point representation and distributed over a relatively broad contact region. The larger effective contact area reduces the local contact pressure beneath the wheel, thereby limiting terrain deformation. By contrast, the pure DEM rock terrain supports the wheel through discrete, localized contacts. The load-bearing area is therefore smaller and more intermittent, such that the same wheel weight is concentrated over fewer contact points. This concentration generates higher local contact stresses, more pronounced particle rearrangement, and a larger displacement response. The mixed rock–sand terrain combines these two mechanisms: the MPM sand phase provides distributed support, whereas the DEM rocks introduce local contact concentration and rearrangement. Its deformation response therefore lies between the continuum-dominated sand case and the fully discrete rock case.

Fig. 10(d) shows the vertical reaction force in the Z-direction acting on the wheel over time. In all cases, the reaction force eventually approaches the quasi-static reference value corresponding to the wheel weight; however, the transient response differs among the terrains because the effective contact area and contact compliance evolve differently. The DEM rock case reaches equilibrium most rapidly owing to its localized, high-stiffness contact network, whereas the MPM sand case evolves more gradually as the load is redistributed over a broader continuum-like region. The mixed terrain exhibits an intermediate response. This interpretation is consistent with previous wheel–soil

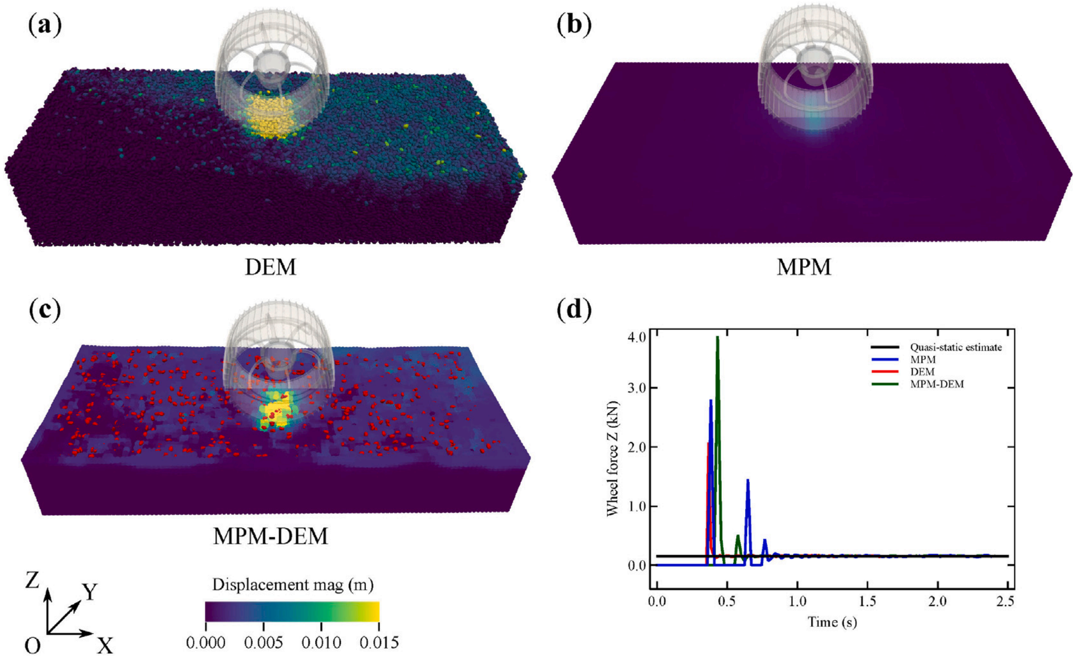

Fig. 10. Displacement fields during wheel drop on three terrain types: (a) Pure rock (DEM), (b) Pure sand (MPM), and (c) Mixed rock–sand (coupled MPM–DEM). Panel (d) shows the wheel vertical reaction force (Z-direction) over the 2.5 s simulation.

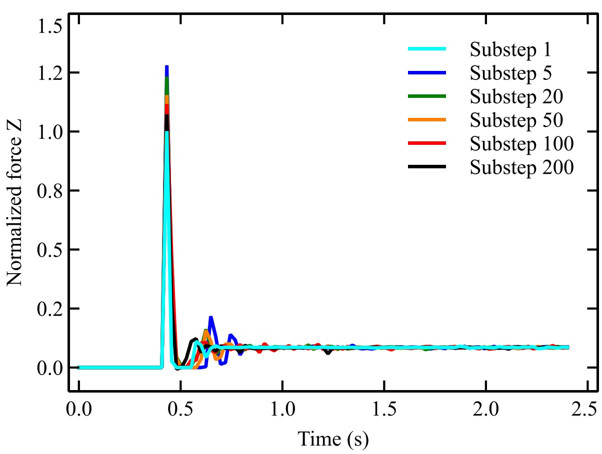

Fig. 11. Normalized contact force during wheel drop on rock–sand terrain with different MPM–DEM substep ratios. The force is normalized by the maximum contact force obtained for the fully synchronized case with a substep ratio of 1 (the substep ratio denotes the number of DEM steps performed within each MPM time step).

studies, which have shown that the mechanical response under the same external loading can vary significantly with the contact medium. In particular, an increased wheel–soil contact area can reduce the local pressure beneath the wheel and modify the apparent radial stiffness. Accordingly, the differences observed here should be attributed not only to the applied wheel load, which is identical in all cases, but also to the manner in which each terrain model distributes that load over the contact region.

To examine the influence of the DEM–MPM substep ratio on the mechanical response, a series of convergence tests was conducted for the wheel-drop problem on rock–sand terrain. The number of DEM steps executed within each MPM step was varied from 1 to 200, and the resulting contact force was normalized by the maximum force obtained in the fully synchronized case, corresponding to a substep ratio of 1 (Fig. 11). The results show that, as the substep ratio increases, the instantaneous impact force generated at the initial wheel–terrain contact first increases and then decreases. By contrast, the stabilized contact force converges to the wheel self-weight for all tested substep ratios. This suggests that the transient impact response is sensitive to the coupling interval between the DEM and MPM solvers, whereas the final quasi-static force balance is preserved.

In the fully synchronized case, the DEM and MPM states are exchanged at every DEM step, resulting in the strongest temporal coupling and increasing the likelihood of resolving short-duration contact interactions. As the substep ratio increases, contact forces are accumulated or averaged over a longer MPM interval before being transferred to the continuum sand phase. This staggered force exchange can introduce additional temporal smoothing and numerical damping in the transient impact response. The observed non-monotonic variation in the peak force therefore reflects the combined effects of contact-force accumulation, delayed MPM feedback, and numerical dissipation during the dynamic impact stage. Considering both computational efficiency and accuracy, a substep ratio of 100 is adopted in the subsequent simulations. This value provides a practical compromise between the fully synchronized case and more strongly staggered cases, while yielding a contact-force evolution close to that obtained with a substep ratio of 1.

3.3. No-slip rolling of a wheel over multiple terrains

This section examines wheel performance during nominal no-slip rolling over four types of terrain: spherical rocks, non-spherical rocks, sand, and mixed rock–sand beds. As illustrated in Fig. 12, the wheel is initially released from rest and allowed to free-fall onto a geostatic terrain bed from a height equal to its diameter, measured from the terrain surface ($\approx$ 0.52 m). During both the geostatic preparation and wheel pre-settling stages, viscous damping is applied to the rock and sand particles to dissipate residual kinetic energy and allow the assembly to reach equilibrium before rolling begins. After impact and settling, a prescribed angular velocity about the y-axis is imposed to initiate rolling. The wheel geometry is based on the *Perseverance* rover wheel, with a radius of approximately 0.26 m, while the terrain domain measures $1.5\ \mathrm{m} \times 0.9\ \mathrm{m} \times 0.6\ \mathrm{m}$. The angular velocity is set to $\omega_y = 0.5$ rad/s and maintained for 10 s using a time step of $5 \times$

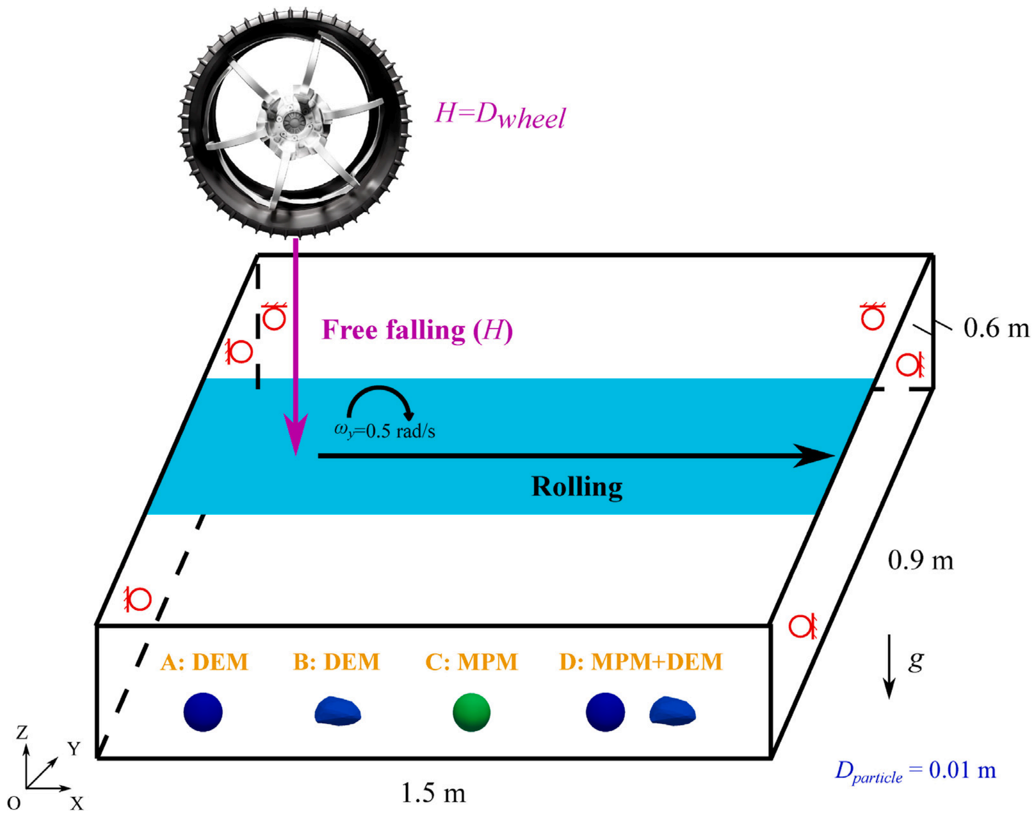

Fig. 12. Wheel interaction with different terrains during initial drop and subsequent no-slip rolling: (a) Spherical DEM rock, (b) Irregular DEM rock, (c) MPM sand, and (d) MPM–DEM rock–sand mixture.

10^{-4} s. Following the observations of Lu et al. (2023), theoretical single-wheel–soil interaction models and its DEM simulation predict that the lateral force remains nearly zero during straight rolling, whereas the driving torque exhibits only minor fluctuations. To reduce the influence of lateral numerical noise on the simulation results, no translational motion is prescribed for the wheel. Instead, forward motion in the positive x-direction develops naturally from the imposed wheel rotation and the resulting wheel–terrain interaction.

The numerical parameters used in the wheel–terrain simulations are summarized in Table 1. The equivalent diameter is defined as the diameter of a sphere with the same volume as the corresponding particle. The wheel density was set such that the wheel load represents one-sixth of the *Perseverance* rover mass, thereby mimicking rover rolling under reduced-gravity loading. The sand phase in the MPM and MPM–DEM terrains was modeled using a Mohr–Coulomb constitutive law. For the numbers of DEM particles and material points listed in the corresponding rows of Table 1, the nonspherical DEM, spherical DEM, MPM, and coupled DEM–MPM simulations achieved computational rates of 73 158 281, and 114 time steps/s, respectively, with memory usage of 4818, 3593, 1754, and 2036 MB.

Fig. 13 shows the stalled wheel position and the terrain displacement field at the end of the 10 s simulation. A notable behavior is observed: on the spherical-rock terrain, the wheel advances a much shorter distance than in the other cases and exhibits a clear *sticking* response. From the perspective of terrain deformation, the spherical-rock case also produces the largest deformation, concentrated primarily beneath the wheel and around the rim due to intrusion and sliding. Consistent with this observation, the wheel on the spherical rock exhibits the greatest sinkage. For the irregular-rock terrain, the strongly non-spherical, angular surface promotes pronounced interlocking. As a result, terrain trapping is less dominant and the wheel reaches a position comparable to that on sand and rock–sand terrain. Nevertheless,

Table 1
Material properties used in the no-slip-rolling wheel simulations.

Parameter \ Terrain	DEM	MPM	MPM–DEM
Equivalent diameter (m)	0.01	0.01	0.01
DEM particles	300 000	–	16 874
Material points	–	101 250	84 376
Wheel density (kg/m^3)	29 453	29 453	29 453
Friction coefficient	0.3	0.3	0.3
Rock density (kg/m^3)	2650	–	2650
Sand density (kg/m^3)	–	1800	1800
Young's modulus, E (Pa)	–	5×10^6	5×10^6
Poisson's ratio, ν	–	0.25	0.25
Friction angle, ϕ (°)	–	25	25
Dilation angle, ψ (°)	–	1	1

the deformation remains substantially larger than in the sand-involved cases, although it is smaller than in the spherical-rock case.

The sand and rock–sand terrains exhibit displacement patterns that differ markedly from those on the rock terrain. In sand (and in mixed sand-rock), the wheel track is characterized by periodically spaced *crinkled* bands, and the induced deformation spreads gradually outward from the track into the surrounding domain. By contrast, displacement in the rock terrain remains strongly localized in the immediate vicinity of the wheel. These differences are consistent with the distinct nature of the media: sand is well represented as a continuum, whereas rock is more appropriately modeled as a discrete assembly. The quantitative wheel kinematics in Fig. 14(a) show that on pure sand the wheel reaches an X-direction velocity close to the ideal rolling prediction, $v_x \approx \omega R$. This performance degrades on the mixed rock–sand and irregular rock terrains, where the X-velocity is reduced by roughly 25%. The spherical rock terrain produces the most pronounced velocity drop, consistent with wheel trapping.

Torque histories in Fig. 14(b) further indicate that any terrain involving rock requires substantially higher torque than pure sand.

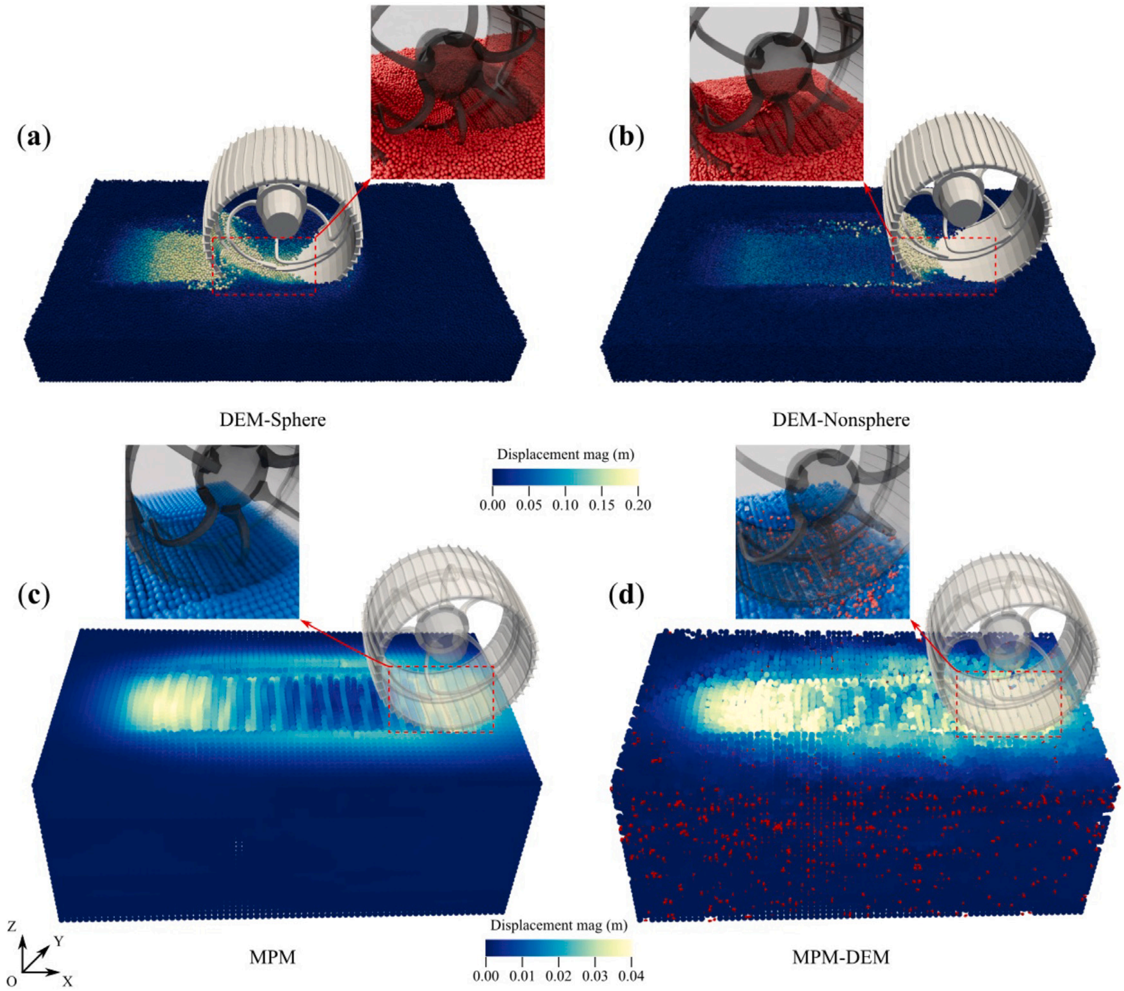

Fig. 13. Magnitude of terrain displacement for: (a) DEM terrain with spherical rocks, (b) DEM terrain with irregular rocks, (c) MPM sand, and (d) coupled MPM–DEM rock–sand mixture. Local configurations are shown in the insets.

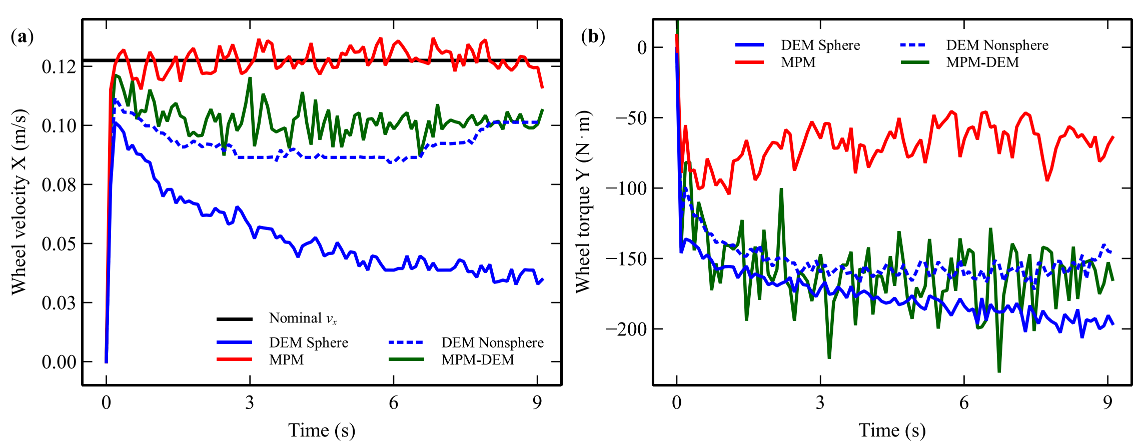

Fig. 14. Time evolution of (a) Wheel velocity and (b) Wheel torque as the wheel rolls over terrains with varying profiles.

Specifically, the torque increases from about 80 kN · m on sand to approximately 170 kN · m with rock present, nearly a twofold rise. Together, these results suggest that pure sand and spherical rock provide practical upper and lower bounds on wheel performance: sand yields the highest attainable translation speed, whereas spherical rock yields the lowest. This also underscores a modeling implication: using a purely continuum approach or a purely discrete approach in wheel–terrain simulation may lead to corner-case predictions that substantially under- or overestimate wheel performance in both dynamics and loading, motivating the use of a coupled method.

3.4. Slip-ratio-controlled wheel rolling in Martian gravity

As discussed in Section 3.3, the prescribed pure-rolling condition provides an idealized reference case, in which the wheel motion is controlled only by its rotational velocity. However, wheel motion on

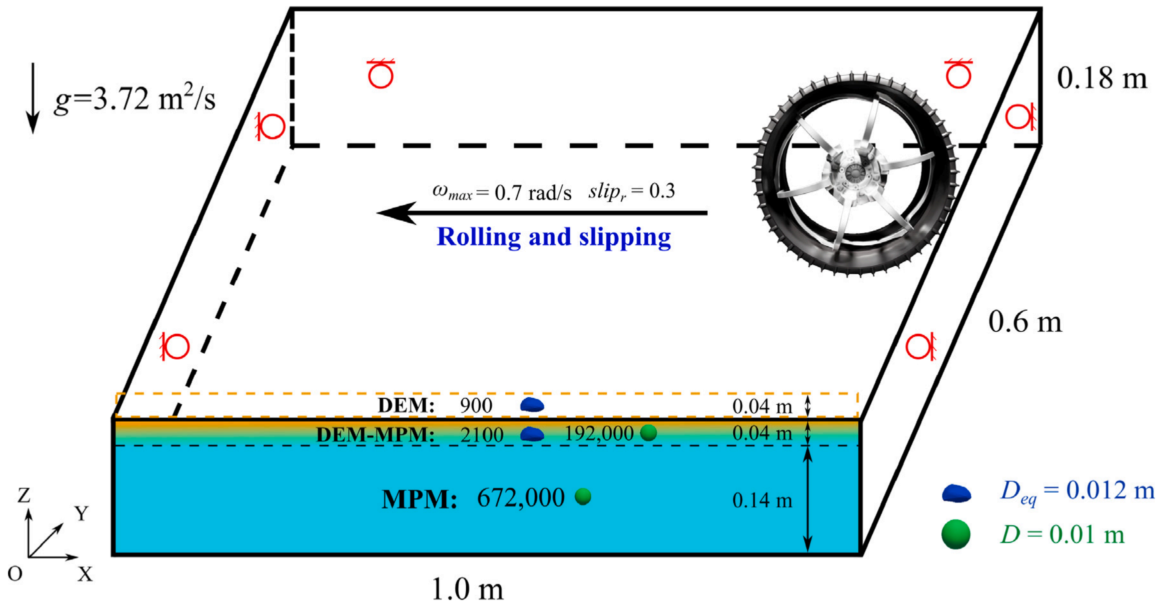

Fig. 15. Configuration of a slip-ratio-driven wheel (slip ratio = 0.3) rolling over terrains under Martian gravity.

heterogeneous rock–sand terrain can deviate from this ideal condition because local particle rearrangement, uneven support, and intermittent wheel–rock interactions may induce slip. To evaluate wheel performance under more realistic mobility conditions, where rolling and slip may occur simultaneously, this section extends the previous pure-rolling analysis by considering mixed slip-rolling cases on a target geology representative of Martian depositional settings. Martian gravity, $g = 3.72\ \mathrm{m/s^2}$, is adopted, and a slip-to-rolling index is introduced based on the slip ratio, $slip_r$, (Wong and Reece, 1967):

$$slip_r = 1 - \frac{v}{\omega r} \tag{15}$$

where v is the translational velocity, ω is the angular velocity, and r is the nominal wheel radius. A higher slip ratio indicates greater driving slip, i.e., substantial wheel rotation accompanied by limited forward translation, which is characteristic of wheel-trapping conditions.

The configuration of the slip-rolling test is shown in Fig. 15. Two terrain types are considered: pure sand and mixed rock–sand terrain. For the pure-sand case, the entire domain $(1.0\ \mathrm{m} \times 0.6\ \mathrm{m} \times 0.18\ \mathrm{m})$ is discretized into 864 000 material points with a uniform spacing of 0.005 m. For the mixed rock–sand case, a layered distribution is employed. The bottom 0.14 m consists of sand, while the overlying 0.04 m forms a transition layer in which 2100 irregular rock particles are generated by randomly replacing material points, thereby mimicking a sand-rock mixture. The topmost layer consists of 900 randomly generated irregular rock particles. All rock particles have an equivalent diameter of 0.012 m.

The slip-rolling phase begins after gravity loading is completed and the wheel–terrain system reaches static equilibrium following wheel settlement. The wheel angular velocity is then ramped to 0.7 rad/s, while the horizontal translational velocity is prescribed to produce a nominal slip ratio of $slip_r = 0.3$. This prescribed slip-ratio condition is used as a controlled numerical setting to isolate the mechanical response of the terrain under combined rolling and slipping motion. In practice, the slip ratio is not directly imposed on a rover wheel; rather, it emerges from the applied drive torque or power and the resulting wheel–terrain interaction. Therefore, the present setup should be interpreted as an idealized numerical test designed to examine the mechanics of slip-rolling interaction under a representative and repeatable slip level. The simulation runs for 3.6 s with a fixed MPM time step of 1×10^{-5} s. The MPM and coupled MPM–DEM simulations required wall-clock times of 4159 and 10 061 s, respectively, corresponding to computational rates of 127 and 53 time steps per second, while maintaining nearly constant memory consumption of approximately 2600 MB.

The wheel represents one of the six wheels of the *Perseverance* rover, as described in Section 3.3; accordingly, its density is set to $29\,453\ \mathrm{kg/m^3}$. The friction coefficient between the wheel and both rock and sand is 0.3. The sand is modeled using a Mohr–Coulomb constitutive law with density $\rho = 1100\ \mathrm{kg/m^3}$, Young's modulus $E = 1 \times 10^7$ Pa, Poisson's ratio $\nu = 0.25$, and friction angle $\phi = 29°$.

A snapshot of the final simulation state is shown in Fig. 16(a) and (b). The most notable difference is the track trajectory in the wake of the wheel. In the pure sand terrain, the grousers produce a pronounced track, whereas no comparable feature is observed in the rock–sand mixture. Instead, the wake is filled with invaded rocks, and some rocks are even deposited along the wheel rim. The lateral (Y-direction) sand flow also differs between the two terrains. In the sand-only case, sand is primarily displaced away from the wheel, with only a weak reverse flow toward the rim, and the surrounding sand remains largely undisturbed. In contrast, the rock–sand mixture exhibits a tendency for the side sand to collapse, and a small portion of the sand extends or bends toward the rim region.

Slices of the terrain at $Y = 0.3$ m, showing the displacement field and the equivalent shear plastic strain-rate field, are presented in Figs. 17 and 18 as a time sequence, where black strokes in columns (b) outline the rock surfaces. Particles (rock and sand) are included in each slice based on their centers of mass. Because the rock phase is sparse and discrete, some rocks may not intersect the slicing plane and therefore do not appear; nevertheless, the slices provide a useful qualitative indication of the overall rock distribution. In addition to these snapshots, Fig. 19 provides quantitative comparisons of velocity and displacement in subfigure (a), and reaction forces and torque in subfigure (b). Overall, the wheel on the rock–sand terrain exhibits only slight sinkage, as indicated by the absence of a pronounced dip in the vertical-velocity curves. At later times, the rock–sand velocity profiles converge toward those of the sand terrain, suggesting that the wheel–terrain interaction approaches a similar steady state for both terrains. Consistent with this trend, the horizontal reaction forces also converge at late times. However, because the wheel sinks more deeply in the sand-only terrain, the corresponding torque is higher.

The displacement and plastic-rate fields clarify why sinkage and reaction forces differ initially but converge at steady state. At $t = 0.5$ s,

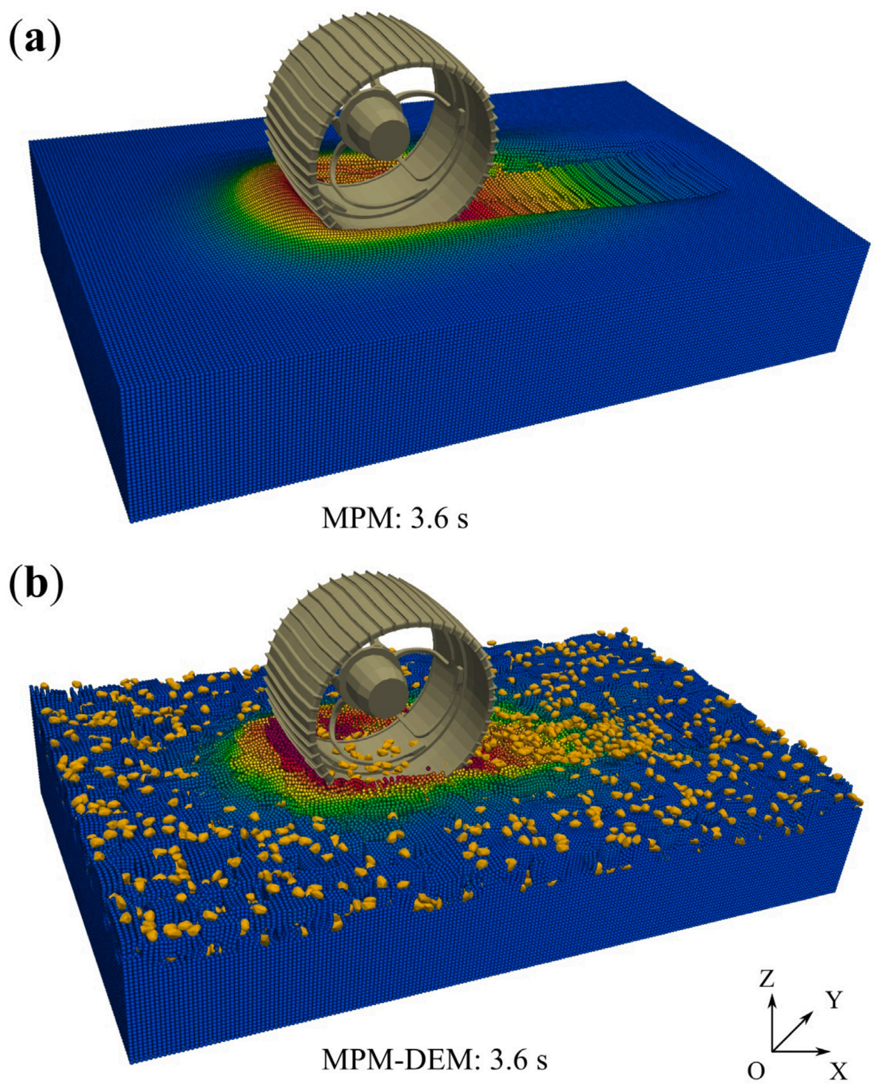

Fig. 16. End-of-simulation snapshots of the slip-rolling tests on two terrains: (a) Pure sand modeled using MPM and (b) rock–sand mixture modeled using the coupled MPM–DEM method.

the displacement pattern closely follows the development of the plastic strain rate. In the sand case, a strong and highly localized plastic zone forms directly beneath the wheel (a thin red band), whereas plastic deformation in the rock–sand terrain is suppressed, as reflected by the lower plastic-rate levels. This confinement of the plastic zone by the rock component limits early sinkage and prevents the sharp initial dip in vertical velocity (approximately $t = 0$ to 0.2 s). From $t = 0.5$ s to $t = 1.5$ s, pronounced wheel slip drives continued rearrangement of the rock phase: rocks migrate from beneath the wheel toward the left boundary of the plastic zone (just outside the highest-rate region), while elevated plastic rates emerge concurrently. This rearrangement increases the horizontal reaction force and produces delayed sinkage as rocks accumulate along the wheel's forward path. Over the full evolution, the failure surface initiates beneath the wheel and propagates toward the left free surface of the terrain. Because the rock content along this dominant failure path is limited, the overall resistance is not controlled primarily by the rock phase, which explains why both terrains ultimately converge to similar velocities and horizontal reaction forces.

4. Simulation example 1: Entrapment of Mars rover *Spirit*

4.1. Background

A well-known mobility failure in planetary exploration is the permanent immobilization of NASA's *Spirit* rover in 2009 at the *Troy* site in Gusev Crater (Lindemann and Voorhees, 2005). During a routine traverse, *Spirit* entered terrain that appeared benign but was later identified as sulfate-rich, fine-grained soil with exceptionally low bearing capacity (Sautter et al., 2015). Under wheel loading, a thin surface crust collapsed, leading to excessive sinkage, slip ratios approaching unity, and a rapid loss of traction. Despite extensive recovery efforts, the rover could not be extricated and ultimately continued operations as a stationary science platform. The *Spirit* entrapment underscores the central importance of soil heterogeneity, large deformation, and wheel–soil interaction mechanisms in rover mobility. The event therefore motivates advanced numerical frameworks that can simultaneously resolve continuum-scale deformation and grain-scale kinematics. In the numerical example that follows, we draw on the *Spirit* scenario to investigate wheel entrapment in a mixed rock–sand terrain, with the goal of reproducing key field-observed features.

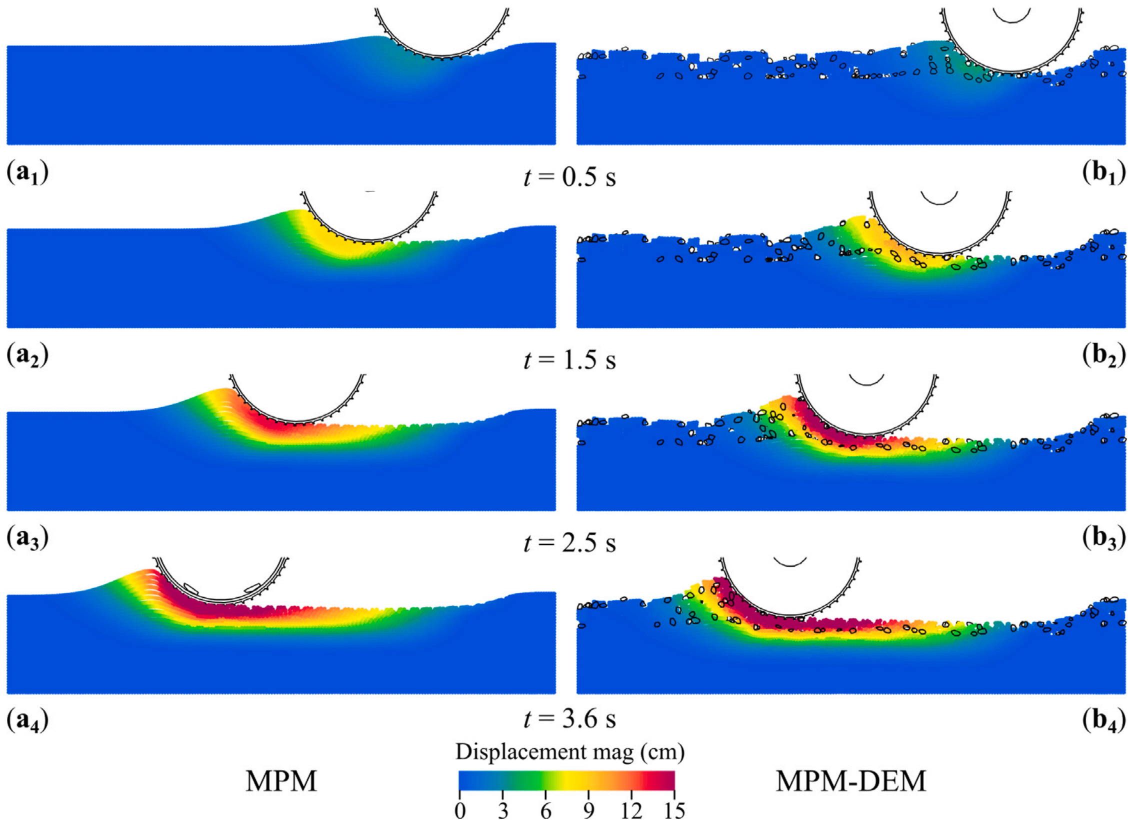

Fig. 17. Displacement fields on the central XOZ plane at selected time instants during wheel rolling on pure sand and rock–sand terrains, column (a): The MPM-simulated sand terrain, and column (b): The coupled MPM–DEM-simulated rock–sand terrain.

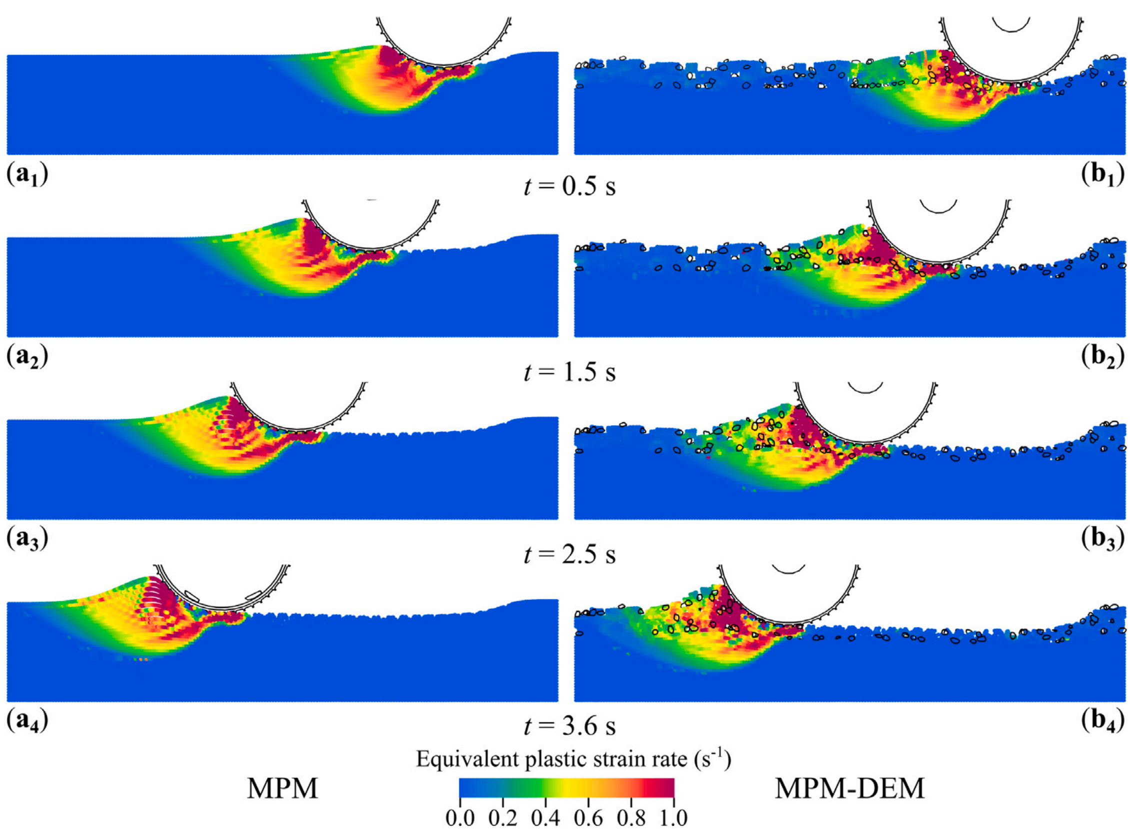

Fig. 18. Temporal development of equivalent plastic shear strain on the central XOZ plane during wheel rolling on the two terrain configurations, column (a): The sand case modeled by MPM, and column (b): The rock–sand case modeled by the coupled MPM–DEM method.

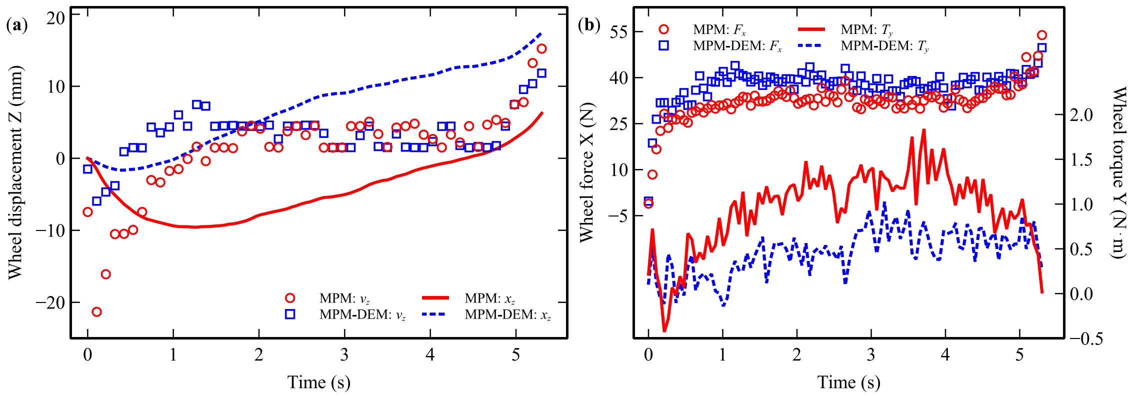

Fig. 19. Time histories of the wheel response: (a) Vertical velocity (markers) and displacement (lines); and (b) Horizontal reaction force (solid lines) and torque about the Y-axis (dashed lines).

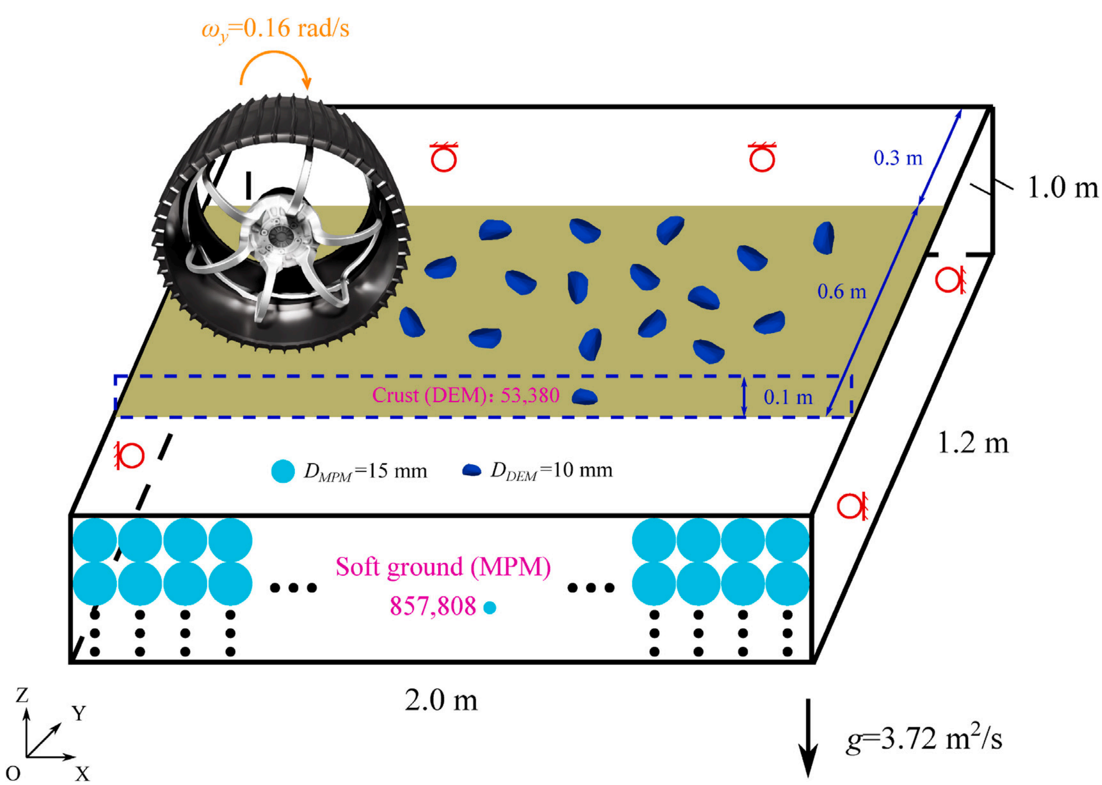

Fig. 20. Numerical setup emulating the crust-over-soft terrain on Mars in which *Spirit* became permanently trapped. The surface crust is represented by DEM particles placed above a soft substrate modeled with MPM. The wheel (representing one of *Spirit*'s six wheels and one-sixth of the rover mass) is driven at a constant angular velocity of 0.16 rad/s, corresponding to the nominal design speed, to emulate an engine-driven attempt to traverse the *Troy* terrain.

4.2. Simulation setup

Fig. 20 shows the numerical setup used to reproduce the *Spirit* rover becoming permanently immobilized on the *Troy* terrain. The deformable regolith is modeled with the MPM, representing an apparently stable yet highly compliant substrate. Material points are spaced at 15 mm, yielding 857 808 points within a 2.0 m × 1.2 m × 1.0 m domain. A crust layer is placed above the soil along the wheel travel direction, with dimensions 2.0 m × 0.6 m × 0.1 m. Within this region, 53 380 rock particles with an equivalent diameter of 10 mm are randomly sampled. This rock diameter represents a computational coarse-particle scale rather than a site-specific mean particle size and is consistent with the coarse clasts observed at Gusev and Gale Craters (Ward et al., 2005; Weitz et al., 2022). The wheel is modeled as a virtual representation of one of the six rover wheels; accordingly, its density is set to 29 453 kg/m^3 to reflect one-sixth of the rover mass. The friction coefficient between the wheel and both rock and sand is set to 0.3. Rock particles are assigned a density of 3000 kg/m^3, while the soft sand is assigned a density of 1600 kg/m^3 (Johnson et al., 2015). The soft substrate is represented by a Mohr–Coulomb constitutive model with Young's modulus $E = 5 \times 10^5$ Pa, Poisson's ratio $\nu = 0.3$, friction angle $\phi = 15°$, and nearly zero cohesion, taken as $c = 100$ Pa to improve numerical stability. Although some discrete-element simulations use an internal friction angle of approximately 30° for Martian soil (Johnson et al., 2015), substantially lower values have been reported for weak surficial materials on Mars. For example, Perko et al. (2006) suggested that the soft soil layer in *Gusev Crater*, where the *Spirit* rover became embedded, may have had a friction angle of 13°–18° and a low cohesion of approximately 600 Pa. Accordingly, the choice of $\phi = 15°$ and $c = 100$ Pa defines a controlled weak-soil condition that promotes pronounced soil yielding, wheel sinkage,

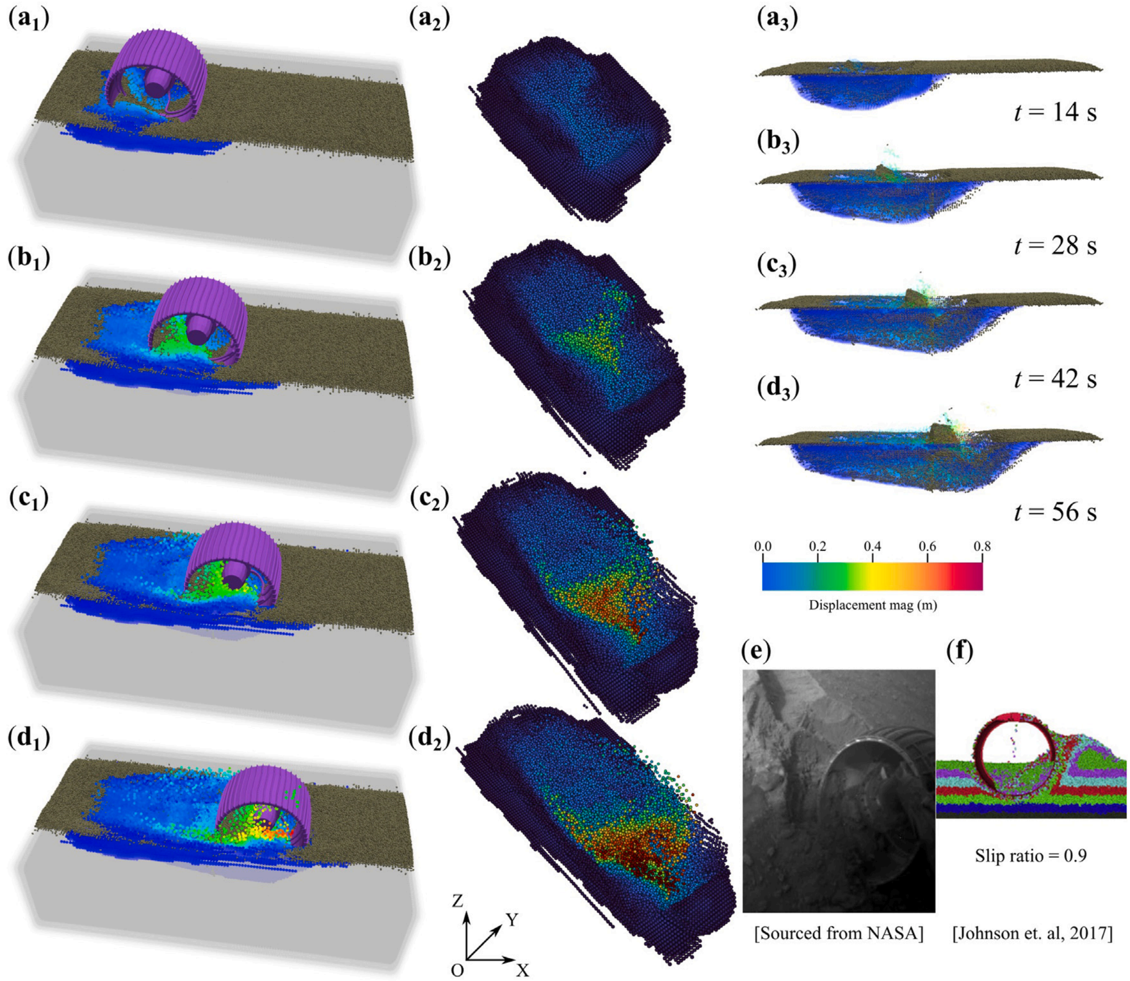

Fig. 21. Snapshots of the *Spirit* rover entrapment scenario. Column (a) shows sand material points with displacement magnitudes exceeding 0.01 m; Column (b) presents a magnified view of the local sand deformation; and Column (c) illustrates the blended rock–sand distribution. Panels (e) and (f) show, respectively, a NASA photograph of the *Spirit* rover entrapment and DEM simulation results reproduced from Johnson et al. (2017).

and trapping behavior, while remaining within a physically defensible parameter range rather than relying on unrealistically weak properties. These parameters are therefore intended to demonstrate the governing mechanisms, rather than to provide a one-to-one calibration of the material at the exact *Spirit* site. Prior to wheel actuation, the terrain (crust and sand) is allowed to settle under gravity. The wheel is then driven using a ramped boundary condition: a nominal wheel speed of 0.16 rad/s is prescribed as an angular velocity about the y-axis to emulate traversal under these ground conditions. The simulation runs for 56 s with a fixed time step of 5×10^{-5} s for the MPM solver. This case required a wall-clock time of 15 774 s, achieved a computational rate of 71 time steps/s, and consumed 2972 MB of memory.

4.3. Results and discussion

The transverse snapshots in Fig. 21 depict the progressive wheel–terrain interaction during entrapment. As the wheel advances, the sand undergoes substantial deformation and is gradually displaced around the wheel, while the DEM rocks are redistributed within the mixed terrain. To reveal the internal material structure, the computational domain is clipped in the side view. The blue displacement envelope represents the deformed sand phase, whereas the brown particles denote the DEM rocks. Accordingly, the rock–sand interface can be interpreted as a transition zone in which the displaced sand envelope and redistributed rock particles coexist. During the early stage ($t < 14$ s), premature immobilization is clearly evident. In the top view (column **b**), a localized displacement field develops near the centerline, and the wheel-rim region becomes filled with both sand and rock particles: rocks accumulate primarily on the X^+ and X^- sides, while sand material points concentrate on the Y^- and Y^+ sides. As the process continues (t = 28–42 s), additional sand material points migrate into the rim region, rocks on the X^+ side are expelled from the rim, and the sinkage rate increases. At the same time, a pronounced sloping surface develops along the lower boundary of the deformed sand domain (column **c**).

The preferential accumulation of rocks along the X^+ rim, followed by their depletion in the immediate contact region, indicates a replacement of rocks by sand: locally, the rock fraction decreases while the sand fraction increases on the X^+ side of the rim. This pattern reflects a squeeze-induced compositional shift. As the wheel advances, rocks initially located near the X^+ rim are displaced upward and forward, while additional rocks may enter the region from the X^-, Y, or Z^- directions. However, this upward–forward migration pathway becomes progressively congested as rocks accumulate into a distinct ridge ahead of the wheel, as shown in the third column. Because rocks are squeezed out faster than they can be replenished or redistributed, the ridge develops into a growing frontal obstacle.

Once a frontal accumulation of rocks has formed, the wheel motion is redirected along the mechanically weaker path. Forward motion is increasingly resisted by the rock ridge, while the material beneath the wheel becomes progressively sand-rich as rocks are displaced outward. Consequently, the imposed wheel motion is accommodated less by forward translation and increasingly by downward penetration into

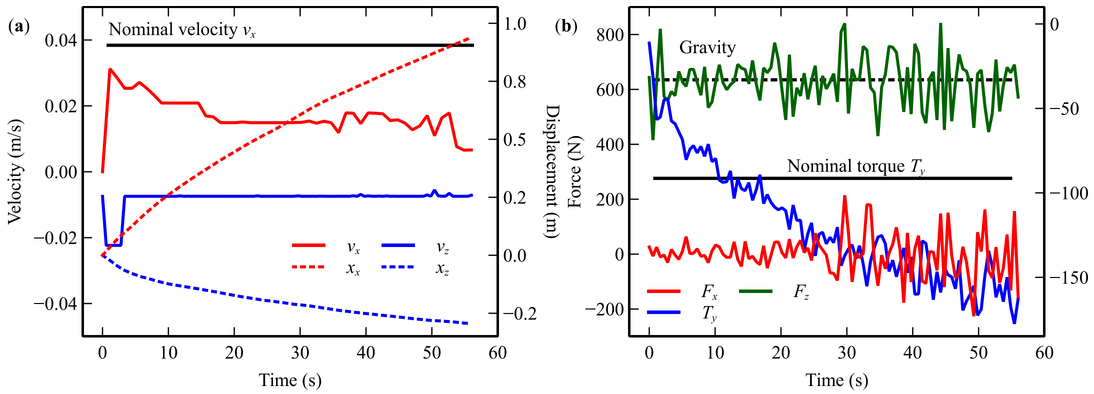

Fig. 22. Time evolution of the *Spirit* rover's velocity and displacement (a), and reaction force and torque (b).

this weakened, sand-dominated region. Around $t \approx 14$ s, this mechanism produces pronounced vertical deformation and wheel sinkage. As motion continues, the frontal obstruction grows, further limiting the ability of the wheel to climb over the accumulated rocks. Simultaneously, the increasing sinkage brings the wheel into contact with more sand-dominated material below, which offers weaker support and further promotes downward motion. This interaction establishes a sinkage-obstruction feedback: the frontal rock accumulation impedes forward motion and drives the wheel downward into the sand-rich zone, while the resulting sinkage further reduces the wheel's ability to overcome the frontal obstacle. Eventually, the wheel becomes immobilized as the imposed driving motion is converted primarily into continued sinkage rather than forward translation.

The evolution of wheel velocity and displacement in Fig. 22(a) further supports the proposed sinkage-obstruction mechanism. Here, v_x and v_z denote the horizontal and vertical wheel velocities, respectively, while x_x and x_z denote the corresponding displacements. During the initial stage ($t < 3$ s), the wheel exhibits substantial forward motion. Shortly thereafter, squeeze-induced resistance develops, as reflected by the rapid decrease in horizontal velocity. In the subsequent stage, v_x continues to decline as sand and rocks are compacted and redistributed around the wheel. The accumulated material in front of the wheel increasingly impedes forward motion, whereas the sand-rich region beneath the wheel provides weaker support and promotes downward penetration. By $t \approx 35$ s, the horizontal velocity fluctuates around a quasi-steady value, while the vertical velocity remains approximately constant. This behavior indicates that the system has reached a dynamic balance among material squeezing, lateral refill, and downward sinkage. In this regime, rocks refilling from the X^-, Y^-, and Y^+ directions partially compensate for material displaced toward the Z^+ ridge direction, resulting in an approximately steady resistive force and nearly stationary mean velocities in both the X and Z directions. The NASA *Spirit* rover entrapment photograph and the corresponding DEM results reported by Johnson et al. (2017), shown in Fig. 21(e) and (f), exhibit features that are highly consistent with the present results. In particular, both cases show soil intrusion into the wheel rim and an extended wheel track associated with reduced mobility. These similarities support the interpretation that wheel immobilization is governed by progressive frontal obstruction and downward sinkage.

For reference, the nominal pure-rolling velocity and traction torque can be estimated as $v_x = \omega R$ and $T_y = \mu W R$, respectively, where ω is the prescribed angular velocity, R is the nominal wheel radius, μ is the friction coefficient, and W is the wheel load. Fig. 23 presents the relationship between the instantaneous slip ratio and the normalized sinkage, with the sinkage scaled by its maximum value. For slip ratios below approximately 0.7, the predicted normalized sinkage agrees more closely with the NASA GRC single-wheel experiments than with the DEM results reported by Johnson et al. (2017). At higher slip ratios, however, the present simulation tends to overpredict the wheel

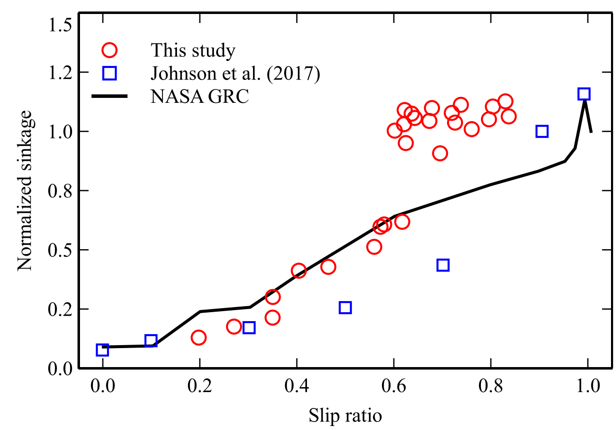

Fig. 23. Normalized wheel sinkage (normalized by its maximum value) as a function of slip ratio for the simulation time series, compared with the NASA GRC experimental data and the DEM results reported by Johnson et al. (2017).

sinkage. The mobilized torque is also approximately twice the nominal estimate, $T_y = \mu W R$, indicating that the wheel experiences additional resistance due to terrain deformation and material accumulation. This discrepancy may be partly attributable to the continuum elastoplastic constitutive model used for the MPM sand phase, which can produce more extensive plastic deformation than the elastic contact-based DEM model employed in the reference simulations. Nevertheless, slip ratios above approximately 0.7 are typically associated with severe mobility loss and unstable wheel–terrain interaction. Thus, despite the overprediction of sinkage in the high-slip regime, the present MPM–DEM framework captures the overall increase in sinkage with slip ratio and provides a reasonable prediction of wheel immobilization behavior.

5. Simulation example 2: Slippery incident of Mars rover *Curiosity*

5.1. Background

Curiosity's ascent toward Mount Sharp in Gale Crater included an attempted crossing of a sandy topographic low informally known as *Hidden Valley*. In this loose, ripple-covered terrain (Mondro et al., 2025; Siminovich et al., 2019), the rover experienced unexpectedly poor mobility, marked by severe wheel slip and little forward progress. The mission team ultimately chose to back out and reroute rather than continue through the valley. Hidden Valley has since become a canonical case in rover-soil interaction research because it illustrates how seemingly safe terrain geometry can conceal conditions that induce large plastic deformation, triggering excessive wheel slip and accelerating drivetrain wear (Rankin et al., 2020). In the numerical

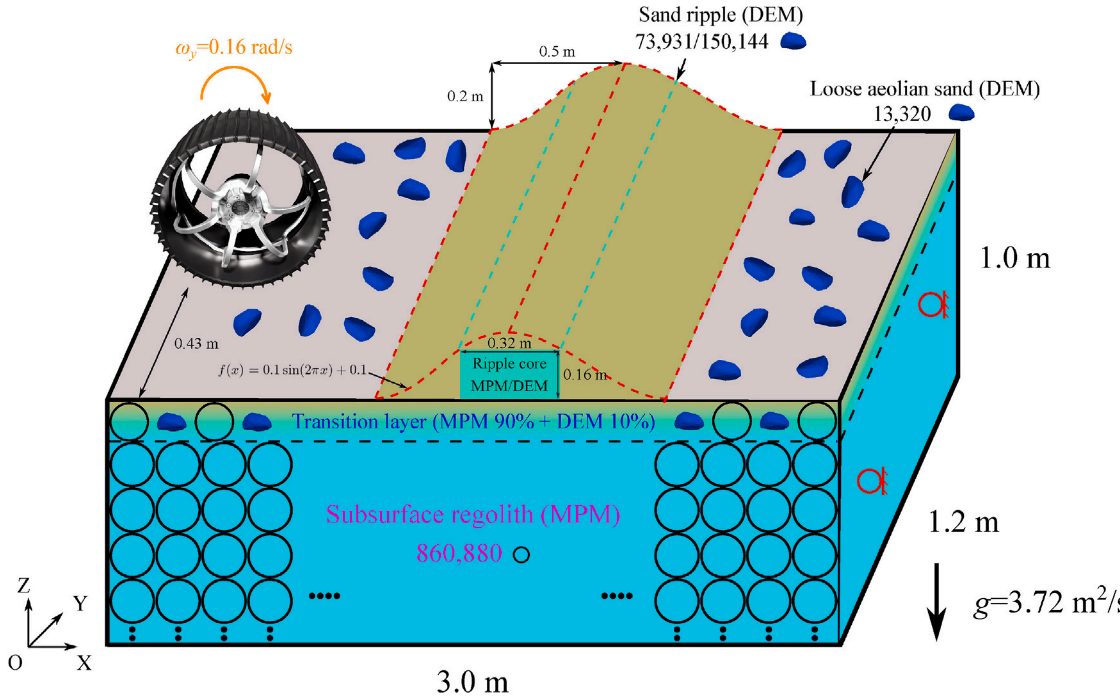

Fig. 24. Numerical configurations for the *Curiosity* rover traversing a sand ripple, determined by the ripple core material, (**core-DEM**): a safe ripple composed entirely of rock; and (**core-MPM**): an apparently safe but hazardous ripple consisting of mixed rock and sand. In both configurations, the ripple overlies a three-layer terrain comprising a subsurface base, a transition layer, and an aeolian surface layer.

example that follows, we use this event to define a *high-slip* benchmark in which a single wheel traverses a deceptively firm-looking surface that is, in fact, a rock–sand mixture with strongly degrading traction. This benchmark enables us to evaluate whether the coupled MPM–DEM model reproduces the key signatures of wheel–terrain interaction observed in the *Hidden Valley* scenario.

5.2. Simulation setup

Fig. 24 illustrates the *Curiosity* rover traversing representative *Hidden Valley* terrain configurations. The regolith is simplified as three layers. The lowermost subsurface layer has relatively high mechanical strength and is modeled as a continuum. Above it lies a transition layer, representing the gradual change from continuum behavior at depth to more discrete surface characteristics, with embedded rock particles. The topmost layer represents the surface, with a higher abundance of distributed rocks to mimic an aeolian, gravelly geomorphic type. A key hazard in *Hidden Valley* is not only the weak substrate but also the presence of widespread aeolian sand ripples formed by persistent winds. These ripples commonly occur in closely spaced trains and can extend over large areas. For simplicity, the present example considers a single ripple and adopts a worst-case geometry, with ripple height up to 0.2 m. The schematic (Fig. 24) is intended for illustration only; the wheel-to-ripple size ratio is not strictly to scale.

To reproduce the terrain that appears strong yet fails readily (thereby yielding mixed predictions for *Curiosity* traction performance), two ripple configurations are considered. The reference configuration is a homogeneous rock ripple composed of 150 144 irregular particles with an equivalent diameter of 10 mm, consistent with the general rock representation adopted in Section 4.2. The ripple surface is prescribed by $f(x) = 0.1\sin(2\pi x) + 0.1$, corresponding to an amplitude of 0.1 m, a peak-to-trough height of 0.2 m, and a wavelength of 1.0 m. The second configuration represents a manually fractured ripple in which the core is replaced by a plastically deformable region, modeled using material points. In this case, 73 931 rock particles remain and 26 260 material points are introduced. The sand core measures $0.32\ \mathrm{m} \times 1.2\ \mathrm{m} \times 0.16\ \mathrm{m}$. The combined rock–sand assembly is first subjected to gravitational settling, after which wheel traversal is initiated.

The wheel density is set to the same value as in Section 4, namely $29\,453\ \mathrm{kg/m^3}$. The rock density in the transition layer, aeolian layer, and ripple is $3000\ \mathrm{kg/m^3}$. Both the base sand and the ripple-core sand are modeled with the Mohr–Coulomb constitutive law, but their properties differ. For the base sand (Arvidson et al., 2017), the density is $\rho_b = 1600\ \mathrm{kg/m^3}$, the Young's modulus is $E_b = 1 \times 10^7$ Pa, the Poisson's ratio is $\nu_b = 0.3$, the friction angle is $\phi_b = 30°$, and the cohesion is zero. For the ripple-core sand, the Young's modulus is $E_r = 5 \times 10^6$ Pa and the friction angle is $\phi_r = 20°$, while all other parameters are identical to those of the base sand. The friction coefficients for wheel–ripple rock, wheel–aeolian rock, and wheel–sand contacts are 0.3, 0.2, and 0.25, respectively. The friction coefficients for ripple rock-ripple rock, ripple rock–aeolian rock, and ripple rock-ripple sand contacts are 0.5, 0.25, and 0.35, respectively. Both terrain and wheel are firstly undergoing geostatic initialization, then the wheel is assigned an angular velocity of 0.16 rad/s to drive toward the ripple. Each simulation runs for 56 s using a fixed time step of 1×10^{-5} s. All terrain and wheel components first undergo geostatic initialization. The wheel is then prescribed an angular velocity of $0.16\ \mathrm{rad\,s^{-1}}$ to drive it toward the ripple. The core-DEM and core-MPM cases achieved computational rates of 75 and 58 time steps/s, required wall-clock times of 74 666 and 98 245 s, and consumed 3205 and 3798 MB of memory, respectively.

Compared with the *Spirit* case in Section 4, for which literature-derived material properties and comparisons with previous studies support a quantitative assessment, the available site-specific properties of the *Hidden Valley* terrain are less well constrained. Accordingly, the *Curiosity* case is intended primarily for trend-level validation and mechanism-oriented reconstruction, rather than for quantitative prediction of absolute sinkage, velocity, force, torque, slip-onset time, or immobilization time.

5.3. Results and discussion

The overall wheel and terrain responses during forward motion are shown in Fig. 25(a–b), respectively. The most notable difference

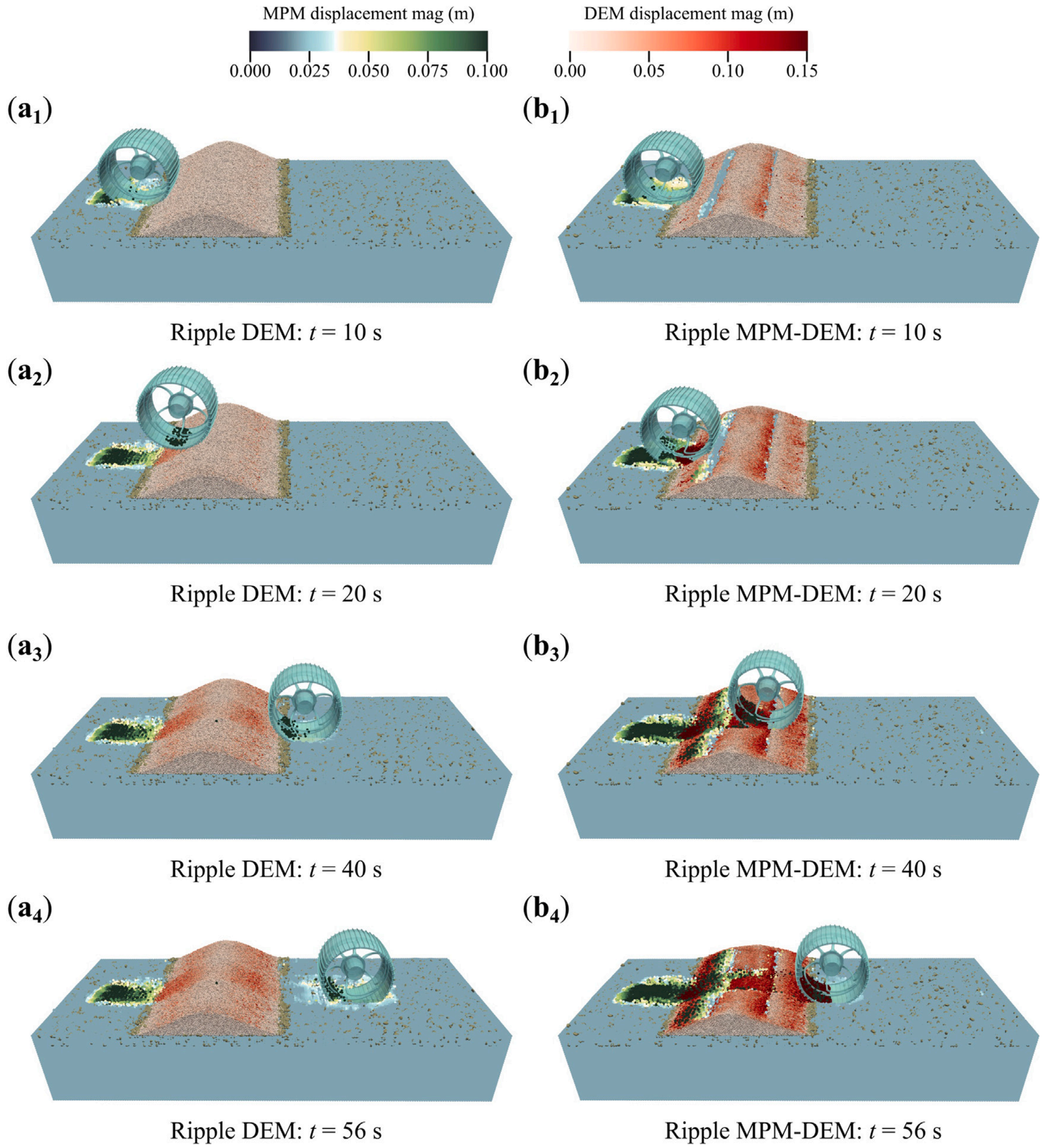

Fig. 25. Wheel traversing two ripples: (a) A safe ripple composed of DEM rock particles, and (b) A deceptively safe yet hazardous ripple represented by a mixture of DEM rock particles and MPM sand material points.

between traversal of the rock ripple and the rock–sand ripple is the earlier onset of wheel slip on the rock–sand ripple. As shown in subfigures ($\boldsymbol{a}_4$) and ($\boldsymbol{b}_4$) at $t = 56$ s, the wheel on the rock ripple comes to rest at a location approximately one wheel diameter from the slope toe, whereas on the rock–sand ripple it stalls near the ripple toe, indicating delayed progression. Consistent with the observed deformation patterns, the rock ripple undergoes no large-scale deformation: displacement remains localized along the wheel track and near the midline on both the upslope and downslope faces. In contrast, the wheel exhibits substantial sinkage while traversing the rock–sand ripple, most prominently near the crest. Consequently, the displacement field develops a banded pattern that spans the ripple length in the Y direction. During the descent, some rocks are entrained by the wheel rim, as shown in subfigures ($\boldsymbol{b}_3$) and ($\boldsymbol{b}_4$).

These deformation differences are also reflected in the wheel velocity profiles (Fig. 26(a, c)). After start-up, the wheel horizontal velocity rises toward the prescribed value (i.e., angular velocity times the nominal radius under pure rolling). However, this target is not fully attained because localized sand deformation around the wheel reduces the effective rolling condition. The horizontal velocity then exhibits a sharp decline in both simulations as the localized deformation propagates and increasingly impedes forward motion. The instant when the wheel reaches the ripple toe is indicated by a clear change in the vertical velocity signal, occurring at approximately 7 s in both cases.

For the rock ripple, both horizontal and vertical velocities increase as the wheel transitions from soft sand onto the rock surface, consistent with a release from deformable support and a more fully mobilized rolling condition. During the subsequent climb and descent over the ripple, the velocity magnitude remains close to the pure-rolling value, as confirmed by the near match to the analytical solution from 27 s to 42 s. Notably, when the wheel passes the downslope region near the ripple toe, a brief slip event is observed: the local velocity decreases, forming a shallow valley in the curve between roughly 46 s and 52 s. This slip rapidly diminishes, and the wheel returns to an approximately pure-rolling state through the end of the simulation (52 s–56 s).

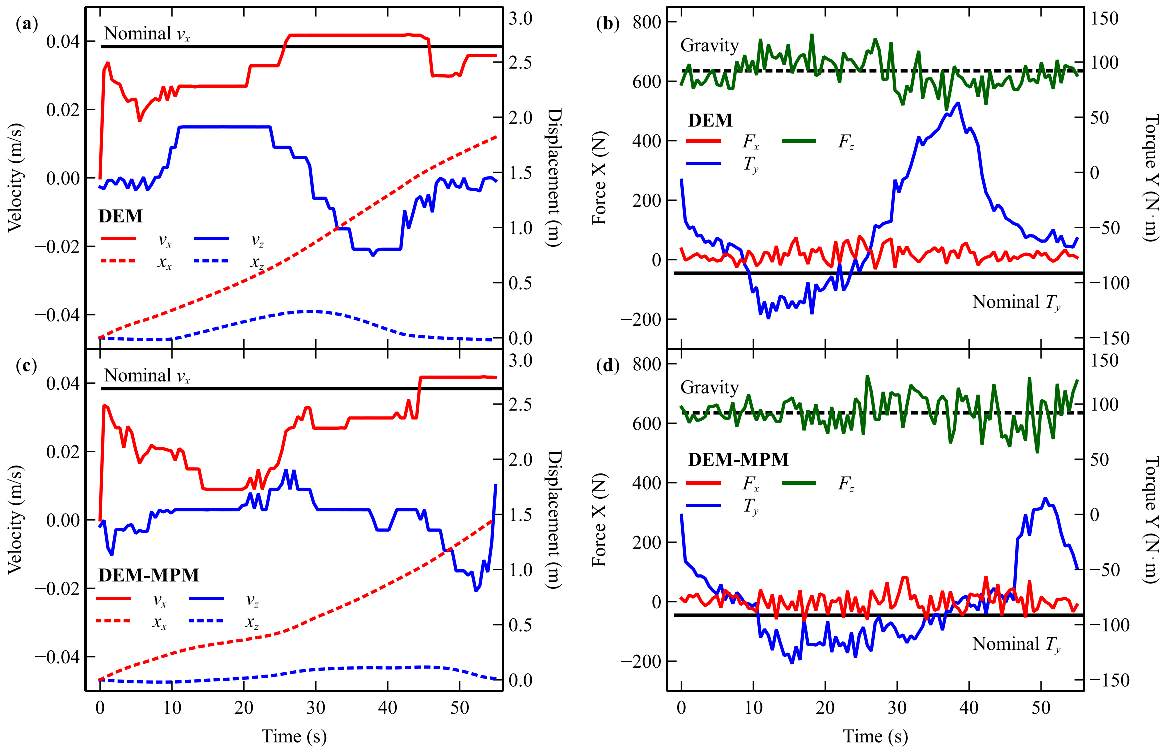

Fig. 26. The development of the wheel's velocity and displacement (a, c), and force and torque as a function of time (b, d).

A different velocity evolution is observed for the rock–sand ripple between 7 s and 23 s. Over this interval, the horizontal velocity decreases continuously while the vertical velocity remains nearly constant. This behavior is interpreted as an approach phase (7 s–15 s) followed by a pronounced slip regime (15 s–23 s), corresponding to the wheel attempting to climb the ripple from its base. Once the wheel is fully on the rock–sand ripple (23 s–42 s), a mild-slip regime persists: the motion is predominantly horizontal (vertical velocity near zero), but the horizontal velocity remains below the analytical pure-rolling prediction. During the descent from the rock–sand ripple, the response returns to near pure rolling, with horizontal velocity closely tracking the analytical solution and no evident slip.

In summary, the rock ripple case exhibits an initial slip, followed by near pure rolling, then a slight slip near the downslope toe, and finally a return to pure rolling; the slip events occur primarily at the base and near the ripple interface. By contrast, the rock–sand ripple produces a sequence of slip regimes: initial slip, serious slip during the climb initiation, mild slip while traversing the ripple, and finally near pure rolling during descent. Comparing the force and torque responses around these slip intervals (Fig. 26(b, d)), the resisting torque in the rock ripple case is approximately -200 N · m during the initial slip and about -75 N · m during the slight slip. For the rock–sand ripple, the initial slip shows a similar resisting torque, but the serious and mild slip regimes correspond to larger resistive levels, approximately -200 N · m and -100 N · m, respectively.

Overall, the rock–sand ripple induces a closely spaced sequence of slip events that, in effect, prolongs the initial slip throughout much of the climbing stage. Moreover, when the wheel leaves the rock–sand ripple, the resisting torque decays more abruptly than in the rock ripple case, indicating a more brittle and discontinuous temporal response. The observed accumulation of rocks near the rim further suggests that the rock–sand ripple poses not only a dynamic challenge to the drivetrain, requiring sustained high power with rapid load fluctuations, but also an increased risk of mechanical degradation due to rim–rock interactions. In a field of repeated ripples, such cyclic loading/unloading combined with rim-region disturbances could significantly threaten rover durability.

6. Conclusions and outlook

This study presents a multiscale wheel–terrain numerical framework for off-road vehicle mobility, with particular emphasis on the durability and stability of planetary rovers operating on heterogeneous terrains. The framework couples a ray-tracing DEM solver, sparse-memory MPM solver, and a novel SDF-based contact solver to enable efficient, cross-length-scale interactions between rover wheels and mixed rock–sand terrains. It captures two-way coupling among wheel–rock (large scale), wheel–sand (small scale), and rock–sand (mixed scale) interactions, while remaining general with respect to wheel geometry, rock morphology, and large-deformation sand behavior. The proposed approach addresses key limitations of conventional experimental and empirical methods, as well as single-paradigm numerical approaches that rely exclusively on discrete or continuum formulations, by enabling concurrent DEM–MPM simulation within a unified framework.

The framework has been thoroughly benchmarked through a series of tests, including SDF-driven DEM–MPM head-on collisions of two spheres, a wheel drop onto mixed rock–sand terrain, and both pure rolling and slip-driven rolling on rock–sand mixtures. When applied to simulate the *Spirit* rover entrapment and the *Curiosity* rover excessive slip cases, this new tool reveals failure mechanisms that are difficult to infer from terrain geometry or empirical models alone. In particular, it identifies a cyclic rock–sand squeezing and jamming process that can evolve into irreversible, permanent entrapment, highlighting how continuum–discrete mixed terrains may immobilize a rover through coupled dynamic and mechanical effects. These results demonstrate strong potential for mobility prediction, stability assessment, and post-incident analysis of off-road vehicles operating in challenging environments. The case studies further show that a highly parallel computing strategy enables scalable simulations across DEM-dominated and MPM-dominated regimes, making high-resolution, engineering-scale analyzes computationally feasible within this framework.

Future work will extend the framework to more complete vehicle models with additional degrees of freedom, including suspension and drivetrain subsystems, and will incorporate additional environmental loadings (e.g., dust storm on Mars) relevant to rover mobility during planetary operations.

CRediT authorship contribution statement

Hao Chen: Writing – original draft, Visualization, Software, Methodology. **Shiwei Zhao:** Writing – original draft, Supervision, Funding acquisition. **Jidong Zhao:** Writing – review & editing, Supervision, Funding acquisition.

Declaration of competing interest

The authors declare that they have no known competing financial interests or personal relationships that could have appeared to influence the work reported in this paper.

Acknowledgments

This work was financially supported by the National Natural Science Foundation of China (Project No. 52439001), the Research Grants Council of Hong Kong (GRF Projects No. 16214525 and No. 16206322, CRF Project No. C7085-24G, and TRS Project No. T22-606/23-R and No. T22-607/24N), and the State Key Laboratory of Climate Resilience for Coastal Cities (SKLCRCC) (via Project ITC-SKLCRCC26EG01). Any opinions, findings, and conclusions or recommendations expressed in this material are those of the authors and do not necessarily reflect the views of the financial bodies.

Data availability

No data was used for the research described in the article.

References

Agarwal, S., Senatore, C., Zhang, T., Kingsbury, M., Iagnemma, K., Goldman, D.I., Kamrin, K., 2019. Modeling of the interaction of rigid wheels with dry granular media. J. Terramech. 85, 1–14.

Andrade, J.E., Chen, Q., Le, P.H., Avila, C.F., Evans, T.M., 2012. On the rheology of dilative granular media: Bridging solid-and fluid-like behavior. J. Mech. Phys. Solids 60 (6), 1122–1136.

Arvidson, R.E., Iagnemma, K.D., Maimone, M., Fraeman, A.A., Zhou, F., Heverly, M.C., Bellutta, P., Rubin, D., Stein, N.T., Grotzinger, J.P., et al., 2017. Mars science laboratory curiosity rover megaripple crossings up to sol 710 in gale crater. J. Field Robot. 34 (3), 495–518.

Bekker, M.G., 1956. Theory of land locomotion. (No Title).

Benatti, S., Young, A., Elmquist, A., Taves, J., Tasora, A., Serban, R., Negrut, D., 2022. End-to-end learning for off-road terrain navigation using the Chrono open-source simulation platform. Multibody Syst. Dyn. 54 (4), 399–414.

Chen, H., Zhao, S., Zhao, J., 2025. A sparse-memory-encoding GPU-MPM framework for large-scale simulations of granular flows. Comput. Geotech. 180, 107113.

Chen, H., Zhao, S., Zhao, J., Zhou, X., 2023. DEM-enriched contact approach for material point method. Comput. Methods Appl. Mech. Engrg. 404, 115814.

Daftry, S., Abcouwer, N., Sesto, T. Del, Venkatraman, S., Song, J., Igel, L., Byon, A., Rosolia, U., Yue, Y., Ono, M., 2022. MLNav: Learning to safely navigate on martian terrains. IEEE Robot. Autom. Lett. 7 (2), 5461–5468.

di Maria, E., Reina, G., Ishii, K., Giannoccaro, N.I., 2021. Rolling resistance and sinkage analysis by comparing FEM and experimental data for a grape transporting vehicle. J. Terramech. 97, 59–70.

Ding, L., Zhou, R., Yu, T., Gao, H., Yang, H., Li, J., Yuan, Y., Liu, C., Wang, J., Zhao, Y.-Y., et al., 2022a. Surface characteristics of the Zhurong Mars rover traverse at Utopia Planitia. Nat. Geosci. 15 (3), 171–176.

Ding, L., Zhou, R., Yuan, Y., Yang, H., Li, J., Yu, T., Liu, C., Wang, J., Li, S., Gao, H., et al., 2022b. A 2-year locomotive exploration and scientific investigation of the lunar farside by the Yutu-2 rover. Sci. Robot. 7 (62), eabj6660.

El-Sayegh, Z., El-Gindy, M., Johansson, I., Öijer, F., 2020. Development and validation of off-road tire-gravelly soil interaction using advanced computational techniques. J. Terramech. 91, 45–51.

Farley, K.A., Williford, K.H., Stack, K.M., Bhartia, R., Chen, A., de la Torre, M., Hand, K., Goreva, Y., Herd, C.D., Hueso, R., et al., 2020. Mars 2020 mission overview. Space Sci. Rev. 216 (8), 142.

Feng, Y., 2021a. An energy-conserving contact theory for discrete element modelling of arbitrarily shaped particles: Basic framework and general contact model. Comput. Methods Appl. Mech. Engrg. 373, 113454.

Feng, Y., 2021b. An energy-conserving contact theory for discrete element modelling of arbitrarily shaped particles: Contact volume based model and computational issues. Comput. Methods Appl. Mech. Engrg. 373, 113493.

Green, J., Hoehler, T., Neveu, M., Domagal-Goldman, S., Scalice, D., Voytek, M., 2021. Call for a framework for reporting evidence for life beyond Earth. Nature 598 (7882), 575–579.

Guo, N., Zhao, J., 2014. A coupled FEM/DEM approach for hierarchical multiscale modelling of granular media. Internat. J. Numer. Methods Engrg. 99 (11), 789–818.

Guo, N., Zhao, J., 2016. Parallel hierarchical multiscale modelling of hydro-mechanical problems for saturated granular soils. Comput. Methods Appl. Mech. Engrg. 305, 37–61.

Guo, X., Zheng, Z., Zang, M., Chen, S., 2022. A multi-sphere DE-FE method for traveling analysis of an off-road pneumatic tire on irregular gravel terrain. Eng. Anal. Bound. Elem. 139, 293–312.

He, R., Sandu, C., Khan, A.K., Guthrie, A.G., Els, P.S., Hamersma, H.A., 2019. Review of terramechanics models and their applicability to real-time applications. J. Terramech. 81, 3–22.

Hu, W., Zhou, J., Serban, R., Negrut, D., 2021. Using an SPH-based continuum representation of granular terrain to simulate the rover mobility. In: International Design Engineering Technical Conferences and Computers and Information in Engineering Conference. Vol. 85468, American Society of Mechanical Engineers, V009T09A028.

Jiang, M., Dai, Y., Cui, L., Xi, B., 2018. Experimental and DEM analyses on wheel-soil interaction. J. Terramech. 76, 15–28.

Johnson, J.B., Duvoy, P.X., Kulchitsky, A.V., Creager, C., Moore, J., 2017. Analysis of Mars Exploration Rover wheel mobility processes and the limitations of classical terramechanics models using discrete element method simulations. J. Terramech. 73, 61–71.

Johnson, J.B., Kulchitsky, A.V., Duvoy, P., Iagnemma, K., Senatore, C., Arvidson, R.E., Moore, J., 2015. Discrete element method simulations of mars exploration rover wheel performance. J. Terramech. 62, 31–40.

Kardani, M., Nazem, M., Sheng, D., Carter, J.P., 2013. Large deformation analysis of geomechanics problems by a combined *rh*-adaptive finite element method. Comput. Geotech. 49, 90–99.

Kawamoto, R., Andò, E., Viggiani, G., Andrade, J.E., 2018. All you need is shape: Predicting shear banding in sand with LS-DEM. J. Mech. Phys. Solids 111, 375–392.

Khan, S.Y., Stack, K.M., Yingst, R.A., Bergmann, K., 2022. Characterization of clasts in the glen torridon region of gale crater observed by the mars science laboratory curiosity rover. J. Geophys. Res.: Planets 127 (11), e2021JE007095.

Li, C., Lewis, K., 2023. The need for and feasibility of alternative ground robots to traverse sandy and rocky extraterrestrial terrain. Adv. Intell. Syst. 5 (3), 2100195.

Liang, W., Zhao, J., 2019. Multiscale modeling of large deformation in geomechanics. Int. J. Numer. Anal. Methods Geomech. 43 (5), 1080–1114.

Lindemann, R.A., Voorhees, C.J., 2005. Mars exploration rover mobility assembly design, test and performance. In: 2005 IEEE International Conference on Systems, Man and Cybernetics. Vol. 1, IEEE, pp. 450–455.

Liu, H., Yao, M., Xiao, X., Cui, H., 2023. A hybrid attention semantic segmentation network for unstructured terrain on Mars. Acta Astronaut. 204, 492–499.

Lu, S., Xu, X., Wang, W., 2023. Coupling dynamic model of vehicle-wheel-ground for all-terrain distributed driving unmanned ground vehicle. Simul. Model. Pr. Theory 128, 102817.

Mardani, A., Ebrahimi, S., Alipour, K., 2020. New adaptive segmented wheel for locomotion improvement of field robots on soft terrain. J. Intell. Robot. Syst. 97 (3), 695–717.

Mondro, C.A., Fedo, C.M., Grotzinger, J.P., Lamb, M.P., Gupta, S., Dietrich, W.E., Banham, S., Weitz, C.M., Gasda, P., Edgar, L.A., et al., 2025. Wave ripples formed in ancient, ice-free lakes in Gale Crater, Mars. Sci. Adv. 11 (3), eadr0010.

Nesnas, I.A., Fesq, L.M., Volpe, R.A., 2021. Autonomy for space robots: Past, present, and future. Curr. Robot. Rep. 2 (3), 251–263.

Nguyen, C.T., Nguyen, C.T., Bui, H.H., Nguyen, G.D., Fukagawa, R., 2017. A new SPH-based approach to simulation of granular flows using viscous damping and stress regularisation. Landslides 14 (1), 69–81.

Niksirat, P., Daca, A., Skonieczny, K., 2020. The effects of reduced-gravity on planetary rover mobility. Int. J. Robot. Res. 39 (7), 797–811.

Peiret, A., Karpman, E., Kovács, L.L., Kövecses, J., Holz, D., Teichmann, M., 2021. Modelling of off-road wheeled vehicles for real-time dynamic simulation. J. Terramech. 97, 45–58.

Peng, C., Li, S., Wu, W., An, H., Chen, X., Ouyang, C., Tang, H., 2022. On three-dimensional SPH modelling of large-scale landslides. Can. Geotech. J. 59 (1), 24–39.

Perko, H.A., Nelson, J.D., Green, J.R., 2006. Mars soil mechanical properties and suitability of Mars soil simulants. J. Aerosp. Eng. 19 (3), 169–176.

Rankin, A., Maimone, M., Biesiadecki, J., Patel, N., Levine, D., Toupet, O., 2020. Driving curiosity: Mars rover mobility trends during the first seven years. In: 2020 IEEE Aerospace Conference. IEEE, pp. 1–19.

Recuero, A., Serban, R., Peterson, B., Sugiyama, H., Jayakumar, P., Negrut, D., 2017. A high-fidelity approach for vehicle mobility simulation: Nonlinear finite element tires operating on granular material. J. Terramech. 72, 39–54.

Ren, S., Zhang, P., Galindo-Torres, S., 2022. A coupled discrete element material point method for fluid–solid–particle interactions with large deformations. Comput. Methods Appl. Mech. Engrg. 395, 115023.

Ren, S., Zhang, P., Zhao, Y., Tian, X., Galindo-Torres, S., 2023. A coupled metaball discrete element material point method for fluid–particle interactions with free surface flows and irregular shape particles. Comput. Methods Appl. Mech. Engrg. 417, 116440.

Sargeant, H.M., Dyson, J., Otto, H., Long-Fox, J., Britt, D., Sheridan, S., 2022. Lunar dust transport from rover wheel interactions: Modelling charged dust grains in surface electric fields. In: 53rd Lunar and Planetary Science Conference. Texas, USA.

Sautter, V., Toplis, M., Wiens, R., Cousin, A., Fabre, C., Gasnault, O., Maurice, S., Forni, O., Lasue, J., Ollila, A., et al., 2015. In situ evidence for continental crust on early Mars. Nat. Geosci. 8 (8), 605–609.

Serban, R., Negrut, D., Recuero, A., Jayakumar, P., 2019. An integrated framework for high-performance, high-fidelity simulation of ground vehicle-tyre-terrain interaction. Int. J. Veh. Perform. 5 (3), 233–259.

Siminovich, A., Elperin, T., Katra, I., Kok, J., Sullivan, R., Silvestro, S., Yizhaq, H., 2019. Numerical study of shear stress distribution over sand ripples under terrestrial and Martian conditions. J. Geophys. Res.: Planets 124 (1), 175–185.

Soga, K., Alonso, E., Yerro, A., Kumar, K., Bandara, S., 2016. Trends in large-deformation analysis of landslide mass movements with particular emphasis on the material point method. Géotechnique 66 (3), 248–273.

Tasora, A., Serban, R., Mazhar, H., Pazouki, A., Melanz, D., Fleischmann, J., Taylor, M., Sugiyama, H., Negrut, D., 2015. Chrono: An open source multi-physics dynamics engine. In: International Conference on High Performance Computing in Science and Engineering. Springer, pp. 19–49.

Verma, V., Maimone, M.W., Gaines, D.M., Francis, R., Estlin, T.A., Kuhn, S.R., Rabideau, G.R., Chien, S.A., McHenry, M.M., Graser, E.J., et al., 2023. Autonomous robotics is driving Perseverance rover's progress on Mars. Sci. Robot. 8 (80), eadi3099.

Wang, X., Lu, Y., Cheng, P., Wen, M., Zhang, Y., 2025. Coupled discrete element-particle analysis of single-wheel and four-wheel off-road vehicle on soft ground. Soil Dyn. Earthq. Eng. 199, 109639.

Wang, Z., Yang, H., Ding, L., Yuan, B., Lv, F., Gao, H., Deng, Z., 2020. Wheels' performance of Mars exploration rovers: Experimental study from the perspective of terramechanics and structural mechanics. J. Terramech. 92, 23–42.

Ward, J., Arvidson, R., Golombek, M., 2005. The size-frequency and areal distribution of rock clasts at the spirit landing site, gusev crater, mars. Geophys. Res. Lett. 32 (11).

Weitz, C.M., O'Connell-Cooper, C., Thompson, L., Sullivan, R.J., Baker, M., Grant, J.A., 2022. The physical properties and geochemistry of grains on aeolian bedforms at gale crater, mars. J. Geophys. Res.: Planets 127 (11), e2021JE007061.

Wiberg, V., Servin, M., Nordfjell, T., 2021. Discrete element modelling of large soil deformations under heavy vehicles. J. Terramech. 93, 11–21.

Wong, J.-Y., Reece, A., 1967. Prediction of rigid wheel performance based on the analysis of soil-wheel stresses part I, Performance of driven rigid wheels. J. Terramech. 4 (1), 81–98.

Xu, X., Yerro, A., Soga, K., Li, M., Jin, F., 2021. Numerical modelling and simulation of the wheel rotation problems by the material point method. In: International Conference of the International Association for Computer Methods and Advances in Geomechanics. Springer, pp. 810–818.

Yamashita, H., Chen, G., Ruan, Y., Jayakumar, P., Sugiyama, H., 2019. Hierarchical multiscale modeling of tire–soil interaction for off-road mobility simulation. J. Comput. Nonlinear Dyn. 14 (6), 061007.

Yamashita, H., Jayakumar, P., Alsaleh, M., Sugiyama, H., 2018. Physics-based deformable tire–soil interaction model for off-road mobility simulation and experimental validation. J. Comput. Nonlinear Dyn. 13 (2), 021002.

Zhang, Y., Gao, Z., Wang, X., Liu, Q., 2023. Image representations of numerical simulations for training neural networks. Comput. Model. Eng. Sci. 134 (2), 821–833.

Zhang, X., Meng, J., Yuan, S., 2022. An implicit nodal integration based pfem for soil flow problems. Comput. Geotech. 142, 104571.

Zhang, X., Zhao, S., Zhang, Z., Bao, L., Guo, Q., 2026. Stiffness-dependent traction behavior of heavy-load flexible wheel in lunar gravity environments. Adv. Space Res.

Zhao, Y., Choo, J., Jiang, Y., Li, L., 2023. Coupled material point and level set methods for simulating soils interacting with rigid objects with complex geometry. Comput. Geotech. 163, 105708.

Zhao, S., Zhao, J., 2023. Revolutionizing granular matter simulations by high-performance ray tracing discrete element method for arbitrarily-shaped particles. Comput. Methods Appl. Mech. Engrg. 416, 116370.

Zhao, S., Zhao, J., Lai, Y., 2020. Multiscale modeling of thermo-mechanical responses of granular materials: A hierarchical continuum–discrete coupling approach. Comput. Methods Appl. Mech. Engrg. 367, 113100.

Zhao, S., Zhao, J., Liang, W., 2021. A thread-block-wise computational framework for large-scale hierarchical continuum-discrete modeling of granular media. Internat. J. Numer. Methods Engrg. 122 (2), 579–608.

Zhao, S., Zhao, J., Liang, W., Niu, F., 2022. Multiscale modeling of coupled thermo-mechanical behavior of granular media in large deformation and flow. Comput. Geotech. 149, 104855.

Zhao, J., Zhao, S., Luding, S., 2023. The role of particle shape in computational modelling of granular matter. Nat. Rev. Phys. 5 (9), 505–525.